Progressive vulnerability of cortical synapses in α-synucleinopathy

Saroj Sah [1,7], Andrew D. Sauerbeck [2,7], Jyoti Gupta [3], Dayana Pérez-Acuña [1,7], Jacob E. Reiber [4], Vijay Singh [4], Dreson L. Russell [4], Thomas M. Goralski [5,7], Michael X. Henderson [5,7], Laura A. Volpicelli-Daley [4,7], Michael J. Higley [3,6,7], Terrance T. Kummer [2,7] and Thomas Biederer [1,7 *]

[1] Department of Neurology, Yale School of Medicine, New Haven, CT 06510, USA
[2] Department of Neurology, Washington University School of Medicine, St. Louis, MO 63110, USA
[3] Department of Neuroscience, Yale School of Medicine, New Haven, CT 06510, USA
[4] University of Alabama at Birmingham, Birmingham, AL 35294, USA
[5] Department of Neurodegenerative Science, Van Andel Institute, Grand Rapids, MI 49503. USA
[6] Department of Biomedical Engineering, Yale School of Medicine, New Haven, CT 06510, USA
[7] Aligning Science Across Parkinson's (ASAP) Collaborative Research Network, Chevy Chase, MD 20815, USA

* Correspondence should be addressed to Thomas Biederer, thomas.biederer@yale.edu

Keywords: Parkinson's disease; dementia with Lewy bodies; Lewy neurites; α–synuclein; synucleinopathy; pre-formed fibrils; cortex; synapse; synaptopathy

ABSTRACT

α-Synuclein aggregates are a hallmark of multiple neurodegenerative disorders, including Parkinson's disease and dementia with Lewy bodies. Cortical pathology in these diseases correlates with cognitive decline. This pathology may progressively impact synaptic connectivity, and we tested this in the frontal cortex in a α-synucleinopathy model. High-resolution imaging showed that intracortical VGLUT1-positive excitatory synapses became increasingly vulnerable, exhibiting early loss near aggregates. The remaining intracortical excitatory synapses were structurally disrupted as measured by high-resolution imaging and electron microscopy. These effects were accompanied by synaptic α-syn accumulation. Ontology analysis of gene expression changes in pathology-bearing neurons showed altered synapse-related processes, with upregulated genes indicating candidate resilience mechanisms. Analyses informed by neuroanatomical connectivity provided additional insights. Mesoscans determined that synapse loss is correlated between cortical layer V and layer II/III, which includes neurons projecting to layer V. Analysis across cortical hemispheres supported a vulnerability of intratelencephalic (IT) projection neurons in layer V. In contrast to intracortical synapses, long-range VGLUT2+ excitatory synapses were spared. Inhibitory VGAT+ synapses were modestly impacted, with a late-stage reduction in postsynaptic specializations. Electrophysiological recordings validated impaired excitatory transmission. This study reveals progressive, synapse-type specific vulnerabilities and resilience and characterizes intracortical synapses as cellular locus of disrupted connectivity in α-synucleinopathy.

INTRODUCTION

Intracellular aggregates of the protein α-synuclein (α-syn) called Lewy neurites and Lewy bodies are a hallmark of synucleinopathies. This pathology is present in the cortex, and symptoms can involve cognitive impairments. This is exemplified by Parkinson's disease (PD), a multiple systems disorder that features not only motor but also prominent non-motor impairments [1, 2]. Up to 80% of patients with PD develop cognitive impairment within 20 years after diagnosis as pathology progresses into cortical areas, and by age 90, 80–90% are affected, with a six-fold increased risk of dementia compared to age-matched healthy controls [3, 4, 5]. Patients can experience cognitive deficits already at early stages, including impaired working memory, visuospatial functions, and difficulties with word recall [3]. In agreement, cortical network dysfunction has been described in PD patients [6, 7, 8], accompanied by a reduction in cortical surface area [6]. Late-stage Lewy pathology in cortical neurons strongly correlates with the extent of cognitive decline and dementia in PD [9, 10, 11, 12, 13]. α-Synucleinopathy in the neocortex is also prominent in dementia with Lewy bodies (DLB) patients [14, 15]. DLB is characterized by cortical vulnerability and intracortical dysconnectivity, and cortical α-syn pathology in DLB correlates with cognitive decline [16, 17, 18, 19].

Misfolded α-syn deposition gradually increases across the brain in PD, including in the neocortex [18, 20]. Pathology propagation across brain regions follows their synaptic connectivity, with non-dopaminergic neuron types in PD exhibiting distinct vulnerability, even in the absence of overt cell death [21, 22, 23, 24]. Synapses are a candidate locus of cellular dysfunction in synucleinopathies [25]. In the healthy brain, α-syn is enriched in presynaptic terminals, and the three members of this protein family shape synaptic architecture [26]. This enrichment may make synapses a neuronal compartment particularly vulnerable to α-syn pathology. Indeed, presynaptic markers are less abundant in PD patients [27, 28, 29], which is correlated with cortical Lewy pathology [30]. Further, the density of dendritic spines, the postsynaptic sites of excitatory inputs, is reduced in several brain regions in PD and models of α–synucleinopathies [31, 32].

We aimed here to define cortical patterns of synaptopathy in the presence of α-syn aggregates. We used the mouse model of intrastriatal α-syn pre-formed fibril (PFF) injections to initiate pathology in cortical projection neurons and analyzed synapses in the frontal cortex at early and at later time points. Key questions were whether synapse subtypes are particularly vulnerable, and the spatial relationship of synaptopathy to α-syn aggregates. The results demonstrate a progressive loss and structural changes of intracortical VGLUT1-positive excitatory synapses while VGLUT2-positive long-range inputs were unaffected. A late-stage increase in isolated VGLUT1-positive pre- and post-synaptic specializations pointed to resilience mechanisms. We also aimed to obtain leads for cellular mechanisms and

determined that synaptic aggregation of α-syn and excitatory synapse loss was first detected in immediate proximity to α-syn aggregates. Ontology analysis of synaptic genes exhibiting altered expression in pathology-bearing cortical neurons pointed to impacted pathways. We additionally used the neuroanatomical connectivity of cortical neurons to understand the appearance of pathology and synapse loss and to identify vulnerable neuron types. Functionally, cortical α-syn pathology impaired excitatory transmission. We obtained these results by applying high-resolution imaging beyond the diffraction limit, electron microscopy, mesoscan imaging, and electrophysiology. This work reveals distinct vulnerabilities and resilience across synapse types in the presence of cortical α-syn pathology.

RESULTS

Intracortical excitatory synapses are progressively lost as α–synuclein pathology appears. How α-syn aggregates impact cortical connectivity is not clearly understood. We tested this using a model where the aggregation of endogenous α-syn is templated by injection of exogenously prepared α-syn pre-formed fibrils (PFFs). PFFs were injected into the dorsolateral striatum of wild-type mice to induce pathology in corticostriatal projection neurons innervating the striatum (Figure 1a). This model allows for precise temporal and spatial control of pathology onset. The exogenously templated α-syn aggregates in the cortex are reminiscent of human Lewy pathology [33, 34] and induce conserved molecular dysfunction as observed in PD patient aggregate-bearing neurons [21]. Cortical spine density is reduced in this model, and excitatory neuron transmission and connectivity are imbalanced [32, 35, 36]. We analyzed the secondary motor area (M2), one of the frontal cortex regions exhibiting pathophysiological changes in synucleinopathies, including PD [37], and selected layer V because of its susceptibility to Lewy pathology [15]. Aggregates characteristic of Lewy pathology were detected immunohistochemically with antibodies against α-syn phosphorylated at S129 (p-α-syn) that detect the misfolded form. Unilateral striatal PFF injection resulted in the templating of endogenous α-syn in the ipsilateral layer V and aggregates became more mature and larger at 3 and 6 months post-injection (MPI) (Supplemental Figure 1), as reported [34, 36, 38]. Injection of α-syn monomer served as a control.

Excitatory synapses were detected by immunostaining for presynaptic VGLUT1, a marker of intracortical synapses, and the excitatory postsynaptic scaffold protein Homer. We performed SEQUIN 3D imaging of synapses in cortical tissue volumes (Figure 1b). This technique employs a multi-detector confocal design to enhance resolution beyond the diffraction limit in all spatial dimensions. This high resolution enables identifying synapses using the criterion that pre- and post-synaptic specializations are paired in space at a distance matching ultrastructurally derived parameters [39].

We tested whether intrastriatal injection of PFFs and the resulting formation of α-syn aggregates in layer V changed synapse density at different pathology stages. No difference in the density of intracortical VGLUT1-positive excitatory synapses was detected at 1 MPI compared to monomer-injected control mice when areas were manually targeted for analysis (Figure 1b,c). Analysis of all individual VGLUT1- or Homer-positive specializations in layer V, which includes synaptically paired and non-synaptic specializations, also showed no change after PFF injection (Figure 1d). At 3 MPI, a significant loss of VGLUT1-positive excitatory synapses was measured in the frontal cortex in PFF-injected compared to monomer-injected mice (Figures 1e,f). Similarly, the density of all individual specializations immunopositive for VGLUT1 or Homer decreased at 3 MPI in PFF- vs. monomer-injected mice (Figure 1g).

This reduction in the density of VGLUT1/Homer-positive synapses persisted at 6 MPI (Figure 1h,i). The analysis of the total number of specializations positive for VGLUT1 or Homer painted a more complex picture than at the 3 MPI timepoint. We observed at 6 MPI in PFF-injected mice an increase in the total number of specializations positive for VGLUT1 or Homer (Figure 1j). This increase in isolated pre- and post-synaptic specializations could be part of a neuronal response to the loss of synapses. The late-stage increase in individual specializations did not compensate for synapse loss, though, as they remained unpaired in space. Together, α-syn pathology in the cortex is associated with a progressive loss of intracortical excitatory synapses and dynamic changes in pre- and post-synaptic specializations.

Excitatory synapses undergo structural changes in the presence of cortical α–synuclein aggregates. We hypothesized that synuclein pathology may impact synaptic morphology in addition to causing the loss of synapses. Using SEQUIN, we measured the pre- and post-synaptic separation of VGLUT1 and Homer specializations in the frontal cortex (Figure 2a). The Gaussian distribution of pre- and post-synaptic distances at synaptic loci showed no change at 1 MPI of PFFs (data not shown). However, at 3 MPI, we detected an increased separation of VGLUT1/Homer specializations after striatal injection of PFFs compared to monomer (Figure 2b,c).

For ultrastructural insights into synapses in the cortex of control and PFF-injected mice, we employed transmission electron microscopy (TEM) (Figure 2d). We previously showed that monomer injections did not produce α-syn pathology [24] or alter the overall structure and abundance of synapses [40] compared to vehicle-injected mice. Thus, PBS injection was used as a control in this study. Mice received injections of PBS or PFFs into the striatum and were perfused for TEM at 3 MPI. Aberrations were found in multiple synaptic compartments in PFF vs. control-injected mice. The synaptic cleft distance was shortened (Figure 2e). This indicated parallel structural disruptions, impacting short-range trans-synaptic interactions on the scale of 20 nm as measured by TEM and the long-range distribution of pre- and post-synaptic protein assemblies on the scale of 300-400 nm as measured by SEQUIN imaging. Presynaptically, the area of individual synaptic vesicles (SV) was modestly but significantly reduced in PFF-injected compared to control mice (Figure 2f). Analysis of inter-SV distance showed a minor reduction in PFF-injected vs. control mice that reached significance, while the number of docked SV and PSD length was unchanged (Supplemental Figure 2). These results demonstrate structural changes in cortical synapses at the same time as synapses are being lost.

Synaptic pathways are dysregulated in p–α–synuclein bearing cortical neurons. Aiming to gain insights into pathways linked to the loss and structural aberrations of synapses in the presence of α-syn

126 aggregates, we analyzed the transcriptome of pathology-bearing neurons compared to those without [21].
127 This dataset was generated for neurons in the frontal cortex of 3 MPI PFF-injected mice and obtained in
128 layers V/VI from the anterior cingulate cortex and the primary and secondary motor cortex. We used
129 SynGO, a synaptic ontology database for gene enrichment analysis of synaptic pathways [41]. 1306 of the
130 1602 SynGO annotated genes were identified in this transcriptomic analysis, confirming deep coverage.
131 Among differentially expressed genes (DEGs), 418 were downregulated and 51 upregulated in
132 pathology-bearing neurons (Figure 3a and Supplemental Figure 3). Analysis of downregulated genes
133 showed that by cellular component, genes of the postsynaptic density and synaptic vesicles were
134 overrepresented (Figure 3b). Biological processes involving these downregulated genes corresponded to
135 synaptic organization, presynaptic vesicle cycle, and processes in the postsynapse (Figure 3c). The
136 expression of markers used for our excitatory synaptic analyses, VGLUT1 and Homer 1, was
137 downregulated. We did not find altered expression of the genes encoding inhibitory VGAT and Gephyrin,
138 which was expected for VGAT as it is expressed in inhibitory neurons, while pathology-bearing cortical
139 neurons are almost exclusively excitatory [21, 24]. Our results of synapse loss and altered morphology in the
140 presence of p-α-syn aggregates are consistent with the downregulation of genes involved in organizing
141 pre- and postsynaptic components and pathways in pathology-bearing neurons.
142 The analysis of upregulated genes pointed to postsynaptic cellular components (Figure 3d).
143 Biological processes associated with upregulated genes included synaptic organization, post-synaptic
144 processes, and synaptic signaling (Figure 3d). This suggests that pathology-bearing neurons are not
145 simply degenerating and losing the ability to express synaptic genes but can also elevate the expression
146 of a subset of these genes, which may increase individual pre- and post-synaptic specialization at later
147 stages (Figure 1j).
148
149 **Phospho-α-synuclein marks excitatory synapses at early pathology stages.** Aggregation of α-syn may
150 disrupt synapses from within, concomitant with gene expression changes. We therefore tested the
151 extent to which cortical synapses are positive for p-α-syn. Aiming to define the early stage of pathology,
152 our analysis was performed at 1 MPI of PFF vs. monomer. Following immunostaining, the pre- and post-
153 synaptic proteins synapsin and PSD-95, respectively, and p-α-syn were imaged using SEQUIN in the
154 frontal cortex (Figure 4a). p-α-Syn was frequently detected in close spatial association within synaptic
155 loci in PFF-injected mice (Figure 4b). We measured the amount of p-α-syn within a 200 nm field around
156 the centroid of each synaptic locus (Figure 4c). As expected, monomer injection did not result in
157 significant immunoreactivity of p-α-syn (Figure 4d). In the PFF-injected cohort of mice, p-α-syn was
158 present at synapses and parenchyma (Figure 4d; $p<0.0001$, linear mixed-effects model). The increase in

synaptic over parenchymal p-α-syn levels marked the synapse-associated amount, showing the synaptic enrichment (Figure 4d; synapse-associated p-α-syn, $p<0.0001$, linear mixed-effects model). Excitatory synapses, therefore, are cellular loci of α-syn pathology.

α-Synuclein pathology matches the extent of synapse loss. We obtained mesoscans across large cortical areas to determine the relationship of synaptic p-α-syn pathology and synapse abundance. This approach allows imaging across scales, visualizing all cortical layers at a super-resolved synaptic level (Supplemental Figure 4). Cortical mesoscans of synapsin, PSD-95, and p-α-syn were collected from 1 MPI animals (Figure 4e,h). Heat maps of synapse-associated p-α-syn and synaptic density were generated for both the monomer and PFF groups (Figure 4f,g and 4i,j). Mesoscans of cortical samples from PFF-injected mice showed increased synaptically localized p-α-syn compared to monomer-injected mice (Figure 4k; $p<0.0001$, linear mixed-effects model). The areas with increased synaptically localized p-α-syn following PFF administration contained fewer synapses (Figure 4l; $p<0.0001$, linear mixed-effects model). These mesoscans covered >180 times more area and identified areas with elevated synaptic pathology for the analysis of synapse density, increasing the ability to determine heterogeneous and spatially specific synaptic effects. This likely explains why the reduction in synapsin/PSD-95-positive excitatory synapses at 1 MPI measured in mesoscans was more pronounced than the trend toward fewer VGLUT1/Homer-positive synapses at the same time point determined by manual, non-targeted imaging (Figure 1b,c). A higher vulnerability of synapsin/PSD-95-positive synapses compared to VGLUT1/Homer-positive synapses cannot be excluded as a reason, though. This data provides evidence that synaptic α-syn pathology is associated with synapse loss.

Synaptic α–synuclein aggregation and excitatory synapse loss are highest close to sites of cortical pathology. We next addressed the spatial relationship between neuritic p-α-syn aggregates and cortical synapse loss at the early stage of pathology at 1 MPI. Synapses were identified using SEQUIN after immunostaining for synapsin and PSD-95. Aggregates immunopositive for p-α-syn were imaged in the same area (Figure 5a,b). The distance of each synaptic centroid to the closest p-α-syn aggregates was measured (Figure 5c). This determined that the labeling for synaptic p-α-syn was highest for synapses proximal to areas containing Lewy neurite-like aggregates, and this was a function of the distance to these aggregates (Figure 5d).

To gain additional insights into the local impact of pathology on synapse loss, we quantified the density of synaptic loci within 800 nm of the perimeter of p-α-syn aggregates and analyzed the extent to which proximal synapse density was related to the relative p-α-syn immunopositivity of the neighboring

192 neuritic aggregates. This determined that synapse loss was most pronounced in the immediate vicinity
193 of aggregates at this early 1 MPI stage of pathology (Figure 5e). The analysis of volumes close to α-syn
194 aggregates therefore revealed areas with early synapse loss at 1 MPI as compared to the trend toward
195 fewer excitatory synapses at this time point determined by non-targeted imaging (Figure 1b,c). These
196 results support that α-syn aggregates locally increase intra-synaptic α-syn aggregation and synapse loss.
197

198 **α-Synuclein pathology does not impact long-range excitatory synaptic inputs.** Aiming to perform a
199 comparative analysis with intracortical VGLUT1-positive excitatory synapses, we performed at 3 MPI
200 SEQUIN imaging of long-range inputs to layer V marked by the presynaptic protein VGLUT2. These inputs
201 predominantly originate from thalamocortical projection neurons, which express VGLUT2. In contrast to
202 VGLUT1-positive synapses, we did not observe changes in the density of the VGLUT2/Homer-positive
203 excitatory synapses in PFF- vs. monomer control-injected mice (Figure 6a,b). We also measured no
204 difference in the number of total VGLUT2-positive puncta, which included specializations paired with
205 Homer and non-synaptic VGLUT2 puncta (Figure 6c). As expected from the prior analysis of Homer
206 immunostainings at 3 MPI (Figure 1g), this independently acquired VGLUT2/Homer data set showed a
207 reduction of total Homer-positive specializations, which included the more abundant VGLUT1/Homer
208 synapses as well as VGLUT2/Homer synapses and non-synaptic Homer sites (Figure 6c). The physical
209 separation of VGLUT2/Homer-positive specializations in excitatory synaptic loci was unchanged (Figure
210 6d-f), as opposed to the increased synaptic VGLUT1/Homer separation (Figure 2a-c). These results
211 demonstrate a specific vulnerability of intracortical VGLUT1-positive synapses in the cortex of this α-
212 synucleinopathy model compared to long-range VGLUT2-positive excitatory inputs.
213

214 **Later-stage α–synuclein pathology is linked to a reduction in cortical inhibitory postsynaptic sites.** We
215 extended our analysis beyond excitatory synapses and determined to what extent inhibitory synapses
216 are affected by α-syn aggregates in the cortex. Immunostaining at 3 MPI for presynaptic VGAT and
217 postsynaptic Gephyrin, followed by high-resolution SEQUIN imaging, did not show an effect of striatal
218 PFF injection on the density of inhibitory synapses comprised of spatially paired VGAT/Gephyrin puncta
219 compared to monomer (Figure 7a,b). No difference in individual VGAT or Gephyrin puncta density was
220 observed at 3 MPI, either (Figure 7c). At 6 MPI, PFF-injected mice also did not exhibit a decrease in the
221 density of inhibitory VGAT/Gephyrin synapses (Figure 7d,e) or the total number of VGAT-positive puncta
222 (Figure 7f). However, mice at 6 MPI had fewer total Gephyrin-positive specializations, including synaptic
223 and non-synaptic sites (Figure 7f). This reduction in the total number of inhibitory postsynaptic

specializations arose months after VGLUT1/Homer-positive synapses had been impacted at 3 MPI, supporting that inhibitory synapses are less vulnerable than VGLUT1-positive excitatory synapses.

Synaptic pathology and loss are correlated across cortical layers. We next asked whether intracortical aberrations occurred in the presence of p-α-syn pathology in layer V. We focused on the relationship with layer II/III, as these neurons primarily project to layer V (Figure 8a). α–Syn pathology was readily detectable in layers V and II/III (Figure 8b). Using cortical mesoscans registered to the Allen Brain Atlas, synaptic loci were identified with SEQUIN in layers V and II/III of the frontal cortex ipsilateral to the striatal injection site. PFF-injected animals exhibited a significant loss of synaptic loci in both layers V and II/III compared to monomer-injected control mice (Figure 8c). Analysis of individual image tiles from layer V or layers II/III supported a loss of synapses in either layer in PFF-injected mice, an effect that was more pronounced in layer V (Figure 8d). While a role of possible projections of layer II/III neurons to the striatum in pathology propagation cannot be excluded, we presume that the projections of layer II/III neurons to layer V underlie this propagation and synaptic loss in layer II/III.

A relationship of pathology and synaptic densities within columns could be expected if their interconnectivity plays a role in pathology propagation (Figure 8e). We tested this in the frontal cortex after striatal PFF injection. We first measured that the distribution of synaptic p-α-syn immunoreactivity in layers V and II/III of individual columns was strongly correlated (Pearson r: 0.654) (Figure 8f). This was higher than the moderate correlation for p-α-syn staining in layers V and II/III in individual columns (Pearson r: 0.469; data not shown). An even stronger correlation than for synaptic p-α-syn was observed for synapse densities in layers V and II/III within the same column (Pearson r: -0.935) (Figure 8g). The extent of synaptic p-α-syn pathology and synapse loss is therefore proportionally shared between interconnected layers V and II/III in the same column.

Contralateral pathology and cortical synapse loss support a vulnerability of IT neurons in layer V. Next, we aimed to use neuroanatomical information to characterize the vulnerability of neuron subtypes. Among cortical projection neurons in layer V, intratelencephalic (IT) neurons project bilaterally to the striatum, unlike ipsilaterally projecting pyramidal tract (PT) neurons (Figure 9a) [42]. We first determined the extent to which α-syn pathology occurred in the cortical hemisphere contralateral to the striatal injection site. We observed the substantial presence of p-α-syn immunopositive aggregates in the contralateral layer V at 6 MPI after unilateral injection of PFFs into the dorsal striatum (Figure 9b). This contralateral pathology replicates earlier data [34].

256 We tested whether this contralateral pathology is associated with changes in excitatory synapse
257 number (Figure 9c). Indeed, SEQUIN imaging of VGLUT1/Homer-positive synapses in layer V
258 contralateral to the striatal injection site showed a significant loss of synaptic loci positive for these two
259 markers at 6 MPI (Figure 9d). The density of individual pre- and post-synaptic puncta was unchanged,
260 indicating that an impairment in their spatial alignment underlies this loss of paired synaptic loci (Figure
261 9e). These results in the hemisphere contralateral to the striatal injection agree with a vulnerability of IT
262 neurons as they project bilaterally and align with the dysregulated gene expression in IT neurons bearing
263 PD pathology [21]. This supports the notion that an imbalance of corticostriatal systems involving IT versus
264 PT neurons contributes to neurodegenerative and other brain disorders [42].
265
266 **α–Synuclein pathology negatively impacts excitatory transmission in the cortex.** Finally, we
267 determined the extent to which these pathology-linked aberrations in excitatory synapse number and
268 structure impact synaptic transmission. We prepared acute cortical slices for electrophysiological
269 recordings 5-6 weeks after striatal injection of PFF vs. monomer control (Figure 10a). Analysis of mEPSCs
270 showed that there was no significant difference in the mean amplitude (monomer group, 11.33±0.88
271 pA, n=8 cells in 3 mice; PFF group, 11.64±0.84 pA, n=12 cells in 6 mice; p=0.81, unpaired t-test) (Figure
272 10b). However, the mean inter-event interval of mEPSCs was significantly higher for PFF-injected
273 compared to monomer-injected control mice (monomer group, 589±191 ms; PFF group, 1413±249 ms;
274 p=0.027, unpaired t-test) (Figure 10c). Analyses of mIPSCs showed no significant differences between
275 groups for either measure (amplitude: monomer group, 16.15±2.01 pA, n=8 cells in 3 mice; PFF group,
276 15.60±1.12 pA, n=9 cells in 6 mice; p=0.81, unpaired t-test; inter-event interval: monomer group,
277 476±107 ms; PFF group, 451±88 ms; p=0.86, unpaired t-test) (Figure 10b,c). This demonstrates impaired
278 excitatory neurotransmission in the cortex under conditions of α–syn pathology.

DISCUSSION

This study demonstrates early glutamatergic synapse loss in the cortex as a sub-cellular locus in α-synucleinopathy. Our approach used the injection of α-syn PFFs into the striatum to track pathology progression in the cortex. This mouse model replicates the abundant α-syn aggregates in human PD biosamples from late-stage patients in cortical layer V [21]. Analyzing the secondary motor cortex as a frontal cortex region, we determined that intracortical excitatory synapses positive for VGLUT1 and Homer in layer V are particularly vulnerable to α-syn pathology. Cortical synaptopathy included not only a loss of synapses but also structural changes in the remaining synapses, suggesting that cortical networks are impacted through parallel synaptic aberrations. These changes are consistent with PD-linked synaptic gene expression changes in pathology-bearing cortical neurons. We additionally observed that excitatory synapses were immunopositive for p-α-syn at early pathology stages when they were proximal to Lewy neurite-like α-syn aggregates, and those areas exhibited the most substantial loss of synapses. The analysis of synapse subtypes determined that long-range VGLUT2-positive synapses did not undergo a loss in the presence of α-syn pathology. Inhibitory postsynaptic aberrations were detected only at the latest stage analyzed. Electrophysiological recordings support that these synaptic changes were functionally relevant and that excitatory transmission was impaired.

Our results support a model where α-syn aggregation within excitatory synapses is linked to loss proximal to α-syn aggregates at 1 MPI, even before the widespread loss of VGLUT1-positive synapses becomes detectable. This is followed by a loss of VGLUT1-positive excitatory synapses in layer V by 3 MPI. In addition to synapse loss, structural changes may render the remaining synapses dysfunctional and unstable. These changes include a spatial separation of pre- and post-synaptic protein assemblies away from synaptic contacts. Furthermore, synaptic vesicles at excitatory cortical synapses were smaller after striatal PFF injection. Our findings complement data that PFF injection into the striatum leads to a redistribution of dendritic spine types and their loss [32, 43]. Interestingly, the progressive reduction in excitatory synapses was observed for intracortical synapses positive for the presynaptic marker VGLUT1 but not VGLUT2-positive synapses, even though they share postsynaptic Homer-positive specializations. This supports that the presynaptic compartment is key to determining synapse vulnerability. At least part of this risk could be conveyed by endogenous presynaptic α-syn, which is abundantly expressed at VGLUT1-positive cortical terminals as shown in projections to the basolateral amygdala, whereas it is scarcely detectable at VGLUT2-positive thalamic inputs [44]. This indicates a pathological role of the presynaptic templating of α-syn, in agreement with the early synaptic p-α-syn aggregation and synapse loss in proximity to aggregates we report here.

311 The reduced expression of synaptic genes controlling synapse assembly and organization, which we
312 report here in pathology-bearing cortical neurons, agrees with the observed structural synaptic
313 pathology. The downregulation of pathways involved in synapse organization identifies candidate
314 targets that may be required for synapse maintenance. Yet, even amid these degenerative processes,
315 synaptic compensation may be an active process that slows synaptopathy. Indeed, the small number of
316 upregulated synaptic genes linked to synapse organization and signaling may be part of neuronal
317 pathways providing resilience. It should be noted that the data for this gene ontology analysis were
318 obtained from pathology-bearing neurons in layer V that are primarily excitatory [21]. Our gene ontology
319 analysis is hence limited to that subtype of cortical neurons and does not include contributions of glia
320 cells or other neuron types.

321 Notably, the changes in excitatory synapses involved dynamic adjustments. Direct synaptic
322 pathology was observed at 3 MPI, when the loss of synapses marked by spatially paired VGLUT1 and
323 Homer sites was paralleled by a decrease in the density of the total number of VGLUT1 and Homer
324 specializations in PFF-injected mice compared to monomer controls. This loss of VGLUT1-positive
325 synapses persisted at 6 MPI, but the density of individual VGLUT1 and Homer specializations
326 unexpectedly increased by that time point. This points to a capacity of neurons to gradually engage
327 compensatory mechanisms to increase the number of pre- and post-synaptic specializations at 6 MPI.
328 Still, the density of synaptic loci identified as spatially paired pre- and post-synaptic specializations
329 remained lower at this time point MPI in PFF- compared to monomer control-injected mice. This may
330 reflect a molecular impairment in the ability of neurons to align pre- and post-synaptic specializations
331 under conditions of α-syn pathology, rendering these specializations as orphan assemblies.
332 Interventions that alter the abundance of trans-synaptic interactions could therefore be targets to
333 restore connectivity and support endogenous resilience mechanisms. There are therefore at least two
334 ways leading to synapse loss in PD, first, a reduction in the number of pre- and postsynaptic sites, and
335 second, an impairment in their alignment.

336 Our results also provide insights into synaptic pathology progression on a circuit level. Our analysis
337 of cortical layers showed the same p-α-syn pathology distribution as reported [21, 35], with aggregates
338 highest levels in layer V but also readily detectable in II/III. The abundance of p-α-syn aggregates in layer
339 II/III was accompanied by excitatory synapse loss and interconnected layers within the same column
340 exhibited a correlated loss of synapses. We could use neuroanatomical connectivity to additionally learn
341 about properties of cellular vulnerability. In the PFF model, IT neurons projecting to the striatum
342 preferentially develop α-syn aggregates following striatal PFF injection [21]. Further, a recent study
343 demonstrated that α–syn pathology is correlated with a loss of dendritic spines in IT neurons in M2 [35].

Our analysis of synapse loss in the layer V contralateral to the striatal PFF injection site is in agreement with a vulnerability of IT neurons as they project bilaterally to the striatum, unlike PT neurons. Together, these results support the model of pathology propagation between synaptically connected neuronal populations. Future studies can now map synapse vulnerability onto different types of pathology-bearing cortical neurons.

The changes in cortical synapses reported here are consistent with decreased functional connectivity in cortical networks in cognitively impaired PD patients [45, 46] and altered cortical circuit connectivity in persons with DLB [17]. Impairments in synapse number, structure, and function in the PFF-based α-synucleinopathy model may contribute to functional deficits, as analyzed in the basolateral amygdala [40]. Indeed, our analysis of the cortex found physiological deficits after striatal PFF injection compared to monomer-injected mice. Specifically, the frequency of miniature EPSC events was reduced in cortical neurons. Related presynaptic changes may involve detrimental effects of pathological aggregates on the endogenous roles of α-syn in the synaptic vesicle cycle [26, 47, 48]. These findings align with results obtained *in vitro* that PFFs alter excitatory synaptic activity in a time- and dose-dependent manner [49] and studies that α-syn aggregation affects excitatory synaptic transmission [43, 50, 51]. Circuit hyperactivity was reported in the somatosensory cortex at 9 MPI of PFFs [52]. This may involve the reduction in inhibitory postsynaptic sites we report here, but can also reflect an emerging intrinsic hyperexcitability of IT neurons [35]. We did not include this late stage in this study because we focused on initial pathology progression. The impaired excitatory transmission we found in the presence of cortical α–syn aggregates can be due to both synapse loss and compromised synaptic function.

Our results reveal distinct, progressive vulnerabilities of cortical synapse types as α-synucleinopathy progresses, and we identify molecular, structural, and functional properties of synaptic impairments. This analysis of cortical pathology supports the notion that synaptopathy is a key process in PD [25, 53] and contributes to cortical dysfunction.

368 ## MATERIALS AND METHODS

369 **Antibodies**. Table 1 provides primary antibodies and application notes for immunohistochemistry (IHC).
370 Secondary antibodies were conjugated to Alexa dyes 405, 488, 568, and 647 (Thermo Fisher). Isotype-
371 specific secondary antibodies were used to detect monoclonal primary antibodies. For mesoscan imaging,
372 the antibody against phosphorylated α-syn was directly conjugated with Alexa-647, as described in the
373 section Tissue processing for cortical mesoscans.
374

Target	Vendor	Cat. No.	RRID	Host	Clonality	Application IHC
VGLUT1	Synaptic Systems	135 304	AB_887878	Guinea Pig	Polyclonal	1:200 (48 h, RT)
VGLUT2	Millipore	AB2251	AB_2665454	Guinea Pig	Polyclonal	1:300 (48 h, RT)
Synapsin 1/2	Synaptic Systems	106004	AB_1106784	Guinea Pig	Polyclonal	1:1000 (72 h, RT)
Homer	Synaptic Systems	160 003	AB_887730	Rabbit	Polyclonal	1:250 (48 h, RT)
PSD-95	Invitrogen	51-6900	AB_2533914	Rabbit	Polyclonal	1:200 (72 h, RT)
VGAT	Synaptic Systems	131 003	AB_887869	Rabbit	Polyclonal	1:250 (36 h, 4 °C)
Gephyrin	Synaptic Systems	147 111	AB_887719	Mouse	Monoclonal IgG1	1:250 (36 h, 4 °C)
pS129 α-syn	BioLegend	825701	AB_2564891	Mouse	Monoclonal IgG2a, κ clone 81A	SEQUIN, 1:2200 (48 h, RT for co-stain VGLUT/Homer; 36 h, 4 °C co-stain VGAT/Gephyrin) Mesoscans, 1:500 (72 h, RT)

375 **Table 1. Primary antibody applications.**
376

377 **Animals**. Mice were injected unilaterally into the striatum, with exception of mice used for preparing
378 electron microscopy samples, which were injected bilaterally. Injections were performed using 3-month-
379 old wild-type C57BL/6J mice (order number #000664, RRID:IMSR_JAX:000664) obtained from Jackson
380 Laboratories (Bar Harbor, ME, USA) and 5-8 weeks old $Snca^{GFP}$ knock-in mice (order number #035412 JAX
381 035412, RRID:IMSR_JAX:035412). Both female and male mice were included in the study unless otherwise
382 stated. All animal procedures undertaken in this study to generate SEQUIN, immunochemistry, electron
383 microscopy, and electrophysiology data were approved by the respective University Institutional Animal
384 Care and Use Committees at Yale University, the University of Alabama at Birmingham, and the
385 Washington University School of Medicine and complied with the National Institutes of Health guidelines
386 for the Care and Use of Laboratory Animals.
387

388 **Preparation of recombinant α–synuclein monomer and preformed fibrils.** Monomeric mouse
389 α–synuclein was expressed in *E. coli* and purified, followed by endotoxin removal using Pierce LAL high-
390 capacity endotoxin removal resin, as previously described [54], with 0.084 EU/µg protein. The monomer was
391 stored at −80°C. Preformed fibrils (PFFs) at a concentration of 5.0 mg/ml were produced from monomeric
392 α-syn by agitation in 150 mM KCl/50 mM Tris-HCl at 37°C for seven days [24, 55]. PFFs in a volume of 22-25

393 µl were placed in a 1.5 ml sonicator tube (Active Motif, NC0869649) and sonicated in a Qsonica Q700
394 sonicator (Newtown, CT) using a cuphorn for 15 min at an amplitude of 30, with a pulse on and off for 3
395 sec and 2 sec, respectively. The required size range of resulting PFF fragments from 20 to 70 nm was
396 verified by dynamic light scattering on a DynaPro NanoStar Dynamic Light Scattering Detector (Wyatt
397 Technology). PFF samples were stored at -80°C until needed. On the day of injection, the sonicated PFFs
398 were thawed at room temperature and re-sonicated in a Qsonica Q700 sonicator for 15 min at an
399 amplitude of 40, with a pulse on and off for 3 s, respectively, at 10°C and used within 8 h. The PFFs were
400 kept at room temperature during the injections. In contrast, the monomer was kept on ice during the
401 series of injections into multiple animals to prevent fibril aggregation and spun at 20,000 x*g* at 4°C with
402 the supernatant used for injections.
403
404 **Stereotaxic injections of α-synuclein monomer and preformed fibrils for SEQUIN and Electron**
405 **Microscopy analyses.** C57BL/6J mice were deeply anesthetized using an isoflurane vaporizer (Harvard
406 Apparatus Mobile Anesthesia System, model 750239) and placed on a stereotactic frame (Kopf, model
407 900 LS). Mice were unilaterally injected with either α-syn monomer or PFFs into the right forebrain at
408 coordinates +0.2 mm relative to Bregma, +2.0 mm from midline, and -2.6 mm beneath the dura to target
409 the dorsal striatum. Injected amounts for SEQUIN and Electron Microscopy analyses were 2.0 µl at 5 µg/µl
410 (Biederer and Volpicelli-Daley laboratories). Injections were performed using a Nanoject III microinjector
411 (Drummond Scientific) at a rate of 20 nl/s over 100 cycles with a delay of 8 s between cycles. The needle
412 remained undisturbed for 10 min after the protein delivery inside the dorsal striatum and was gradually
413 withdrawn to prevent backflow or leakage into the cortex. The skull was closed using sutures, and the
414 mice were placed on a heating pad to recover until they regained consciousness and were returned to
415 their home cages.
416
417 **Stereotaxic injections of α-synuclein monomer and preformed fibrils for electrophysiological analysis.**
418 For slice electrophysiology, 5-8 week old $Snca^{GFP}$ knock-in mice were anesthetized with isoflurane in a
419 chamber, mounted in a stereotaxic frame, and continually maintained under isoflurane anesthesia using
420 a vaporizer (Harvard Apparatus). Anesthetized mice were unilaterally injected with either monomer or
421 PFF in the right dorsal striatum using the coordinates 0.2 mm posterior to Bregma, 2.0 mm lateral to the
422 midline, and at a depth of 2.6 mm from the dura. Injected amounts of either α-syn monomer or PFFs for
423 electrophysiological analyses were 1.6 µl at 5 µg/µl (Higley laboratory). Injections were performed using
424 a Nanoject III microinjector (Drummond Scientific) at a rate of 20 nl/s over 80 cycles with a delay of 7
425 seconds between cycles. The pipette was left in place for 10 minutes after the injection to prevent
426 backflow while withdrawing. The incisions were sealed with sutures, and the mice recovered on a heating
427 pad until they were conscious. The mice were then returned to the colony and used for experiments 5-6
428 weeks post-injection.
429
430 **Tissue processing for synapse quantification.** Synaptic loci of the prefrontal cortex were analyzed in layer
431 V of the secondary motor cortex M2. We processed tissue for SEQUIN imaging as described, with
432 modifications [39, 56]. In brief, mice injected with either monomer or PFFs were analyzed at 1, 3, or 6 months
433 post-injection. Mice were deeply anesthetized by intraperitoneal ketamine (100 mg/kg) and xylazine (10
434 mg/kg) cocktail injection and transcardially perfused using a 27G needle at a rate of 6 ml/min with ice-
435 cold 1x Phosphate Buffered Saline (PBS) for 4 min, followed by ice-cold 4% formaldehyde (PFA) in PBS (pH
436 7.6) for 4 min. The brains were then extracted and post-fixed for 24 h at 4°C in 4% PFA in PBS and stored
437 in PBS at 4°C in scintillation vials protected from light. Fixed brains were sectioned coronally into 40 µm
438 thick slices using a vibratome (Leica VT1000 S). Brain slices were stored in 24-well plates in cryoprotectant
439 buffer (PBS containing 30% ethylene glycol, 30% sucrose, and 0.02% sodium azide) at −20°C.
440 Slices with prefrontal cortex were washed 3 times for 5 min each in PBS, then blocked in 20% normal
441 goat serum (Jackson ImmunoResearch) in PBS for 1 h at room temperature (RT). Slices were then
442 immunolabeled with primary antibodies and washed 3 times for 5 min each in PBS, followed by Alexa

443 Fluor-labeled secondary antibodies prepared in PBS containing 10% NGS and 0.30-0.45% Triton X-100 in
444 the dark (details on antibodies used and conditions are listed in Table 1). Sodium azide (0.02–0.05%) was
445 added during primary and secondary antibody incubation. The slices were washed 3 times for 5 min each
446 in PBS to remove the unbound secondary antibodies, counterstained with DAPI in PBS for 10 min, rinsed
447 3 times for 5 min each in PBS, transferred to charged microscopic glass slides, dried at RT, and rinsed in
448 distilled water to remove PBS residues. The slides were dried at RT and embedded in mounting media
449 freshly prepared by mixing Tris-MWL 4-88 (Electron Microscopy Sciences #17977-150, Hatfield, PA, USA)
450 with AF300 (Electron Microscopy Sciences #17977-25) in a 9:1 ratio. High-precision No. 1.5H cover glasses
451 with a thickness of 170 µm ± 5 µm were used (Marienfeld # 0117580). The cover glasses used for SEQUIN
452 were stain-free, thoroughly cleaned with 100% ethanol, rinsed with distilled water, and air-dried prior to
453 coverslipping. The slides were cured at RT for 3 days.
454
455 **Synaptic imaging and analysis.** Images for synaptic analyses were obtained, processed, and analyzed as
456 previously described [56] using a Zeiss LSM 900 Airyscan Microscope (Carl Zeiss Microscopy) with 63x
457 (numerical aperture 1.4) oil immersion objectives (6-10 images per animal from 3 slices) and processed in
458 3D Airyscan. The channel alignment of the Airyscan-processed images co-stained with VGLUT1 and Homer
459 was corrected for a minor chromatic aberration of 1.0-1.2 pixels using Zeiss ZEN 2.3 SP1 (Black). This
460 correction did not affect the comparison of synaptic loci analysis between PFF- and monomer-injected
461 mice. A chromatic aberration correction was not necessary for other types of synaptic analysis, as
462 determined by visual inspection. Pre- and post-synaptic puncta were detected using Imaris 3D
463 visualization software (Bitplane), and individual puncta and synaptic loci where they were aligned were
464 quantified through a custom nearest neighbor analysis in MATLAB version R2023b. The custom MATLAB-
465 based code is available on GitHub: https://github.com/KummerLab/SEQUIN.
466 To quantify synapse density, the frequency distribution of nearest-neighbor pre- and post-synaptic
467 protein pairs was generated for the top 20% intensity of pre- and post-synaptic puncta. For the
468 VGLUT2/Homer1 synaptic loci analysis, the top 60% most intense pre- and post-synaptic puncta were used
469 due to the lower number of VGLUT2. Most VGLUT2 puncta were nearest neighbors to Homer. The
470 frequency distribution of nearest neighbor pairs, which forms a Gaussian distribution and excludes all
471 random non-synaptic pairings, was used to calculate the synaptic locus density. The mean value calculated
472 at the peak of the Gaussian distribution provided the average pre-post synaptic separation. The number
473 of pre- and post-synaptic puncta, including those randomly allocated and not associated with synaptic
474 loci, irrespective of whether they were within synaptic loci, was quantified from the spot analysis using
475 Imaris 3D visualization software, version 10.2.
476
477 **Synuclein pathology progression analysis.** Mouse cortical slices obtained at 1, 3, and 6 months post-
478 injection of PFF into the striatum were co-stained for DAPI and phosphorylated α-synuclein (pS129 α-syn).
479 Ipsilateral cortical sections, i.e. from the same side where PFF was injected into the striatum, were used
480 to analyze synuclein pathology. Tiled cortical images were acquired using a spinning disk Dragonfly
481 microscope (Andor–Oxford Instruments) equipped with a Zyla CMOS camera and a 20× air objective. The
482 stitched 3D images with z-stacks of 10 µm were analyzed using IMARIS 3D visualization software (v10.2,
483 Oxford Instruments). The surface module was used to quantify the intensity and size of p-synuclein
484 aggregates (surface detail, absolute intensity, and threshold), as previously described for the volumetric
485 quantification of synuclein pathology [57].
486
487 **Tissue processing for cortical mesoscans.** Tissue staining for cortical mesoscans was performed using
488 SEQUIN [39, 56] with slight modifications. Prior to the application of primary antibodies, sections were rinsed
489 with phosphate-buffered saline (PBS) and then blocked with 20% normal goat serum (Vector Labs S-1000)
490 in PBS with 0.3% Triton X-100 (Sigma-Aldrich X100) and 0.05% sodium azide for 1 hour. The blocking
491 solution was then replaced with primary antibodies in 10% normal goat serum in PBS with 0.3% Triton X-
492 100 (Sigma-Aldrich X100) and 0.05% sodium azide for 3 days. To reduce the possibility of off-target

labeling when performing mouse-on-mouse staining, the antibody directed against phosphorylated α-syn was preconjugated to Alexa-647 using Thermo Alexa Fluor™ 647 NHS Ester (Succinimidyl Ester) (Thermo cat# A20006) and purified using Zeba spin desalting columns (Thermo Cat# 89883). Following primary incubation, tissue sections were thoroughly rinsed, and then the secondary antibodies Goat anti-Rabbit 568 (Thermo cat# A-11011) and Donkey anti-Guinea Pig 488 (Jackson ImmunoResearch Cat# 706-545-148) were applied and incubated overnight. The following day, sections were thoroughly rinsed, and the nuclear counterstain DAPI was applied. Sections were rinsed again and then mounted on charged slides and coverslipped with Mowiol 4-88 + AF300 (9:1 ratio, Electron Microscopy Sciences, #17977-150 and #17977-25) and 1.5h coverslip (Marienfeld # 0107242).

Acquisition of cortical mesoscans and image analysis. Images for analyses of synapses on population levels were acquired using a Zeiss LSM 980 microscope using the 8Y multiplex scanning mode, allowing for increased scanning speed while maintaining sufficient super-resolution imaging capabilities to perform synaptic localization analysis. Regions of interest were outlined in Zen Blue, and a 3x3 array of focus points was generated. At each focus point, the center of the z-stack was manually set to the center of the tissue section, and a horizontal plane focus map was created. Every section was imaged with identical microscope imaging parameters. During each imaging session, images from a 'Channel Alignment' section were acquired for the measurement and correction of chromatic aberration [56]. Following the acquisition, images were Airyscan processed using 3D mode with a strength of 4.0.

Image analysis was performed using https://github.com/KummerLab/SEQUIN. Since the SEQUIN-based selection of loci is intensity-based and allows for direct within-animal comparisons across regions, for each tile scan, the 5th percentile of intensity for each synaptic channel was calculated prior to spot detection and then applied to all tiles. Once the synaptic loci had been identified, all subsequent metadata was obtained from the raw imaging data. To improve the identification and separation of synaptic and non-synaptic pairs during SEQUIN analysis, a gradient-boosting machine learning classifier was trained using LightGBM [58] available at https://github.com/microsoft/LightGBM, and metadata on the colocalized pre- and post-synaptic loci from original SEQUIN based methods. Direct comparison of the machine learning classifier versus previous SEQUIN methods revealed matching results for standard intensity cutoff ranges. Notably, the classifier was able to separate the primary synapse peaks from the entire dataset even as dimmer puncta were included in the analysis, similar to two-Gaussian deconvolution, while also maintaining the identity of each punctum which is required for all subsequent analyses in these studies.

Quantification of synapse-associated p-α-syn was performed on synaptic loci identified using SEQUIN. All images received a fixed cutoff background subtraction of the p-α-syn labeling, calculated from monomer treated animals which do not exhibit prominent p-α-syn aggregation and are thus a measure for non-specific labeling. For each synaptic pair of pre- and post-synaptic puncta, a 200 nm field was defined around the centroid and the intensity of the p-α-syn channel was measured. The parenchymal intensity of p-α-syn was quantified using the intensity of p-α-syn outside of Lewy neurites but within the same image field. For the comparison of synaptic and parenchymal p-α-syn levels in PFF treated animals, given the regionally specific aggregation patterns of p-α-syn, the top 20% of tiles by p-α-syn level were identified for analysis. These tiles were manually verified to represent the areas with prominent p-α-syn aggregation. Statistical analysis of mesoscan data involving multiple cortical areas was performed using a linear mixed-effects model (fitlme) in MATLAB version R2023b. This approach accounted for the requirement for repeated imaging from the same animal and allowed for animal and region of interest to be specified as random effects during the analysis. Heatmaps of synaptic density and p-α-syn levels were generated for each animal and registered to a common reference section using a landmark-based affine registration (ImageJ, NIH). Registered heatmaps for each group were combined to generate final group-wise heatmaps.

For quantification of synapse-associated p-α-syn as a function of distance to Lewy neurites, p-α-syn-positive neurites were first masked. Neurite masks were generated by using a size exclusion difference-

of-gaussian filter followed by an intensity cutoff equivalent to the 95th percentile of p-α-syn intensity for areas of high pathology, allowing for uniform detection of neurites across areas of differing magnitudes of pathology and treatments. For each synaptic centroid, the nearest voxel within a masked Lewy neurite was then measured. For each masked Lewy neurite, the intensity of p-α-syn within the neurite mask was measured, then the mask was dilated 800 µm, and the density of synaptic loci within the dilated area was quantified. The dilation radius of 800 µm corresponds to the average neurite-synapse separation distance and is the separation distance where increased synaptic p-α-syn begins to be detected.

Quantification of synaptic alterations within cortical columns was performed using a combination of atlas registration for identification of cortical layers using QuickNII and VisuAlign available at https://scicrunch.org/resolver/RRID:SCR_017978, followed by a semi-automated segmentation of cortical columns. Cortical layers were identified following section-specific registration to the Allen Brain Atlas. Layer-specific alterations in synaptic density were analyzed with a Mann-Whitney test on layer-specific sub-regions of individual imaging tiles, to ensure that only synaptic loci from the specific cortical layer of interest were included in the analysis. The boundaries between layers I vs II/III and layers II/III vs V of the entire secondary motor cortex M2 were traced manually and five cortical columns per animal were identified. Given that cortical column and layer specific ROI boundaries could subdivide individual z-stack tiles, only tiles that maintained at least half of their image were kept. To ensure correlations were performed on sufficient imaging data, only cortical columns that contained at least two image tiles were included in the analysis.

Electron microscopy and image analysis. Electron microscopy and image analysis were conducted as described previously [40]. Briefly, male mice (n=4 PBS, n=4 PFF) were anesthetized using isoflurane and perfused with phosphate buffered saline (PBS) followed by 2.5% glutaraldehyde and 2% paraformaldehyde (pH 7.5). Brains were fixed in 2.5% glutaraldehyde and 2.0% paraformaldehyde in PBS for 2 hours at room temperature and then transferred to 4°C for 16 h. Embedding was performed using 2% 255-bloom calf skin gelatin with 3% agarose in PBS. A vibratome was used to cut 200 µm sections followed by dissection of M2 cortex, and immersion in 2% paraformaldehyde in 0.1 M cacodylate buffer at pH 7.4. The samples were shipped in 0.1 M phosphate buffer to the Center for Cellular and Molecular Imaging EM Core facility at Yale Medical School.

Post-fixation was performed using 1% OsO4 and 0.8% potassium ferricyanide in 0.1 M cacodylate followed by en bloc staining with 2% aqueous uranyl acetate, dehydration in a graded series of ethanol up to 100%, substituted with propylene oxide, and embedded in EMbed 812 resin (Electron Microscopy Sciences, Hartfield, PA). Following polymerization of sample blocks at 60°C, 60 nm sections were cut using a Leica ultramicrotome (UC7) and post-stained with 2% uranyl acetate and lead citrate. Imaging was performed with FEI Tecnai transmission electron microscope at an 80 kV accelerating voltage, and digital images were acquired with an AMT NanoSprint15 MK2 camera (Advanced Microscopy Techniques, Woburn, MA).

Asymmetrical synapses were quantified by a researcher blinded to experimental conditions. Synapses were excluded from analysis if they exhibited a poorly defined postsynaptic density (PSD), if the PSD signal was so intense that it obscured both membranes, if the presynaptic terminal contained fewer than 4 synaptic vesicles, or if synapses were at the edge of the frame. A convolution neural network trained on mouse synapses was utilized to measure the area of individual synaptic vesicles [59]. For the measurement of synaptic cleft width, the two edges of the PSD adjacent to the presynaptic terminal were determined, and the distance between the PSD and presynaptic membrane was measured at the midpoint between these two edges. The PSD was manually traced using ImageJ, and the length was measured using the segmented line tool.

For statistical analyses, the 5% minimum and 5% maxima were trimmed because histograms revealed right-skewed data, and a Box-Cox transformation was applied. Data were analyzed using a linear mixed model with mouse number as "subjects" and synapse number as repeated measures; compound symmetry variance structure was used with treatment as a fixed effect.

GeoMx data quality control, normalization, and analysis. In the mouse GeoMx experiment, 124 segments were collected in total from 11 mice, and 21 of these segments failed Quality Control (QC) analysis and were removed from the dataset. One segment was removed for sequence stitching < 80%, and aligned sequence reads < 75%. Five additional segments were removed for aligned sequence reads < 75% alone, and four segments were removed for sequence saturation < 50%. An additional 11 segments were removed for < 3% of genes being detected above the Limit of Quantification (LOQ). Of the 20175 gene targets contained in the GeoMx Mouse Whole Transcriptome Atlas, 9035 were included in the downstream analyses following QC analysis. 1 gene target was removed as a global outlier (Grubbs test, P<0.01), and 7 were removed as local outliers (Grubbs test, P<0.01). 211 genes were detected below the limit of quantification and were removed. Of the remaining gene targets, 9,031 were detected above the LOQ in at least 10% of segments and therefore were selected for further analysis. An additional 4 gene targets were identified as interesting *a priori* and were retained in the study for analysis. Detailed QC parameters are described in https://github.com/Goralsth/Spatial-transcriptomics-reveals-molecular-dysfunction-associated-with-cortical-Lewy-pathology (DOI: 10.5281/zenodo.10732492). The Sample size was determined based on pilot data. No statistical method was used to determine sample size. Experiments did not involve multiple experimental conditions.

In the human GeoMx experiment, 238 segments were collected in total from 8 human PD/PDD/DLB cingulate cortex samples (n=6 male, n=2 female). The Human GeoMx data was assessed on the same parameters as the mouse tissue for QC. In total 63 segments failed QC and were removed from the dataset. 33 samples were removed for low sequence saturation, and 6 segments were removed for low area. An additional 24 segments were removed for < 5% of genes being detected above LOQ. Of the 18,815 gene targets present in the GeoMx Human Whole Transcriptome Atlas, 8,601 gene targets were included in the downstream analyses following QC. 9 gene targets were removed as local outliers (Grubbs test, P<0.01). 138 genes were detected below the limit of detection and were removed. Of the remaining gene targets, 8,595 were detected in at least 10% of segments. 6 gene targets were identified as interesting *a priori* and were retained in the study for additional analysis. Detailed QC parameters are described in our human analysis pipeline https://github.com/Goralsth/Spatial-transcriptomics-reveals-molecular-dysfunction-associated-with-cortical-Lewy-pathology (DOI: 10.5281/zenodo.10732492). Sample size was determined based on pilot data. No statistical method was used to determine sample size. Experiments did not involve multiple experimental conditions.

To account for systematic variation between AOI's, we normalized each count by the 75th percentile (Q3) of expression for each AOI. To ensure normalization and Quality Control (QC) procedures were accurate, we compared each AOI's Q3 value to its limit of quantification. Normalization and QC procedures were determined to be adequate for robust downstream analysis.

Differential expression of gene targets in the GeoMx experiments was determined via a mixed effects linear regression model. The regression model implemented was as follows:

*(1) y= gene ~ comparison of interest * variable to control + (1/individual)*

This model robustly tests for differential gene expression for comparisons of interest (e.g. p-α-syn negative vs. p-α-syn positive brain region differences) while controlling for confounding variables and multiple sampling of the same samples.

Gene Set Enrichment Analysis was implemented using the GSVA [60] (RRID:SCR_021058) package in R to determine disrupted pathways between neurons positive and negative for p-α-syn immunoreactivity. The minimum pathway size was set to 5 genes, and the maximum pathway size was set to 500 genes. We utilized Kegg Brite pathways to determine which transcriptional pathways are differentially expressed.

For cell-type deconvolution, we used nanoString's SpatialDecon algorithm [61] to determine the cell-type proportions in our spatial transcriptomics data. We determined cell-type proportions in our data via comparison of our data to single-cell atlas data from the Allen Brain Institute via SpatialDecon's log normal regression. To determine the statistical significance of differences in cell type proportions between inclusion-bearing (p-α-syn immunopositive) and non-inclusion bearing (p-α-syn immunonegative) segments, we utilized the following equation:

642 *(2) y= cell-type proportion ~ inclusion status group + (1/individual)*
643
644 **GeoMx data availability.** The raw sequencing files and associated metadata for both mouse and human
645 experiments generated in this study have been deposited in the Sequence Read Archive (SRA):
646 https://www.ncbi.nlm.nih.gov/sra/PRJNA1082339
647 The pre-quality control and supporting data for all experiments are available at the following Zenodo
648 repository: https://zenodo.org/records/10729767 (DOI: 10.5281/zenodo.10729767)
649
650 **GeoMX code availability.** Code used to generate and analyze gene expression and cell detection is
651 available on GitHub: https://github.com/Goralsth/Spatial-transcriptomics-reveals-molecular-
652 dysfunction-associated-with-cortical-Lewy-pathology (DOI: 10.5281/zenodo.10732492).
653
654 **SynGO enrichment analysis.** The expert-curated SynGO gene ontology database [41] was used to
655 characterize the GeoMX-derived synaptic transmission pathways enriched in differentially expressed
656 genes from p-α-syn bearing neurons available from Goralski et al. [21]. The list of DEGs was loaded against
657 the 1602 annotated genes (SynGO release 1.2 '20231201'). For downregulated genes (enriched in p-α-syn
658 immuno-negative neurons), 418 genes were mapped (397 genes had a cellular component annotation,
659 and 299 had a biological process annotation). For upregulated genes, 51 were mapped, with 46 having a
660 cellular component annotation and 34 a biological processes annotation. Additionally, 40 and 18 cellular
661 component terms and 82 and 15 biological processes were significantly enriched at 1% FDR for
662 downregulated and upregulated genes, respectively.
663
664 **Electrophysiology.** Mice injected with monomer or PFFs as described above were at 5-6 weeks post-
665 injection deeply anesthetized with isoflurane and transcardially perfused with oxygenated (95% O_2/5%
666 CO_2) ice-cold choline artificial cerebrospinal fluid (Choline ACSF) containing (in mM): 110 choline, 25
667 $NaHCO_3$, 1.25 NaH_2PO_4, 2.5 KCl, 7 $MgCl_2$, 0.5 $CaCl_2$, 20 glucose, 11.6 sodium ascorbate, 3.1 sodium
668 pyruvate. The perfused mice were decapitated, and the brains were quickly removed for acute slice (300
669 µm thick) preparation from the injected (PFF or monomer) hemisphere. Acute slices were prepared in the
670 coronal plane from the region neighboring the injection site, and the recordings were conducted from the
671 primary somatosensory cortex. Slices were incubated in warm ACSF (32°C) containing (in mM): 127 NaCl,
672 25 $NaHCO_3$, 1.25 NaH_2PO_4, 2.5 KCl, 1 $MgCl_2$, 2 $CaCl_2$, and 20 glucose bubbled with 95% O_2/5% CO_2. After
673 incubating at 32°C for 30 minutes, the slices were stored at room temperature (RT). Whole-cell recordings
674 were carried out at RT from layer II/III pyramidal cells located in proximity to GFP-labeled fibrils. Pyramidal
675 cells were identified under differential interference contrast by their pyramidal somatic shape and
676 prominent apical dendrite. Series resistance was maintained at less than 25MΩ and uncompensated.
677 Recordings were made using a Multiclamp 700B amplifier (Molecular Devices), filtered at 2 kHz, and
678 digitized at 10 kHz using custom software [62]. To record miniature postsynaptic currents, 1 µM tetrodotoxin
679 (TTX) was added to the bath. Glass electrodes (3.0-3.5 MΩ) were backfilled with an internal solution
680 containing (in mM): 126 cesium gluconate, 10 HEPES, 10 sodium phosphocreatine, 4 $MgCl_2$, 4 Na_2ATP, 0.4
681 Na_2GTP, 1 EGTA (pH 7.3 with cesium hydroxide). Cells were voltage-clamped at -70mV to record miniature
682 excitatory postsynaptic currents (mEPSCs) and at 0mV to record miniature inhibitory postsynaptic
683 currents (mIPSCs).
684

ACKNOWLEDGMENTS

We would like to acknowledge Dr. Tina Matos for her contribution as our ASAP Project Manager, Dr. Sreeganga Chandra for input on the project design and the manuscript, and Pranav Shedge for technical support. We thank Dr. Xinran Liu, Department of Cell Biology, Yale School of Medicine, for enabling the EM work as Director of the Electron Microscopy Core Facility. This research was funded by Aligning Science Across Parkinson's ASAP-020616 (to TB, LV-D, MJH, MXH, TKK) through the Michael J. Fox Foundation for Parkinson's Research (MJFF) with additional support from NIH grant R01 DA018928 (to TB). For open access, the author has applied a CC BY public copyright license to all Author Accepted Manuscripts arising from this submission.

AUTHOR CONTRIBUTIONS

All authors conceived approaches. S.S. performed mouse injections and performed and analyzed immunohistochemical studies; A.D.S. performed immunohistochemical studies, optimized imaging approaches, and developed and optimized image quantification; J.G., electrophysiological recordings; D.P.-A., transcriptomic data analysis; J.E.R., V.S., and D.L.R., preparation and quality control of PFFs; T.M.G., transcriptomics data; M.X.H., supervised T.M.G. and manuscript input; L.A.V.-D., supervised V.S., J.E.R., D.L.R. and manuscript input; M.J.H., supervised J.G. and manuscript input; T.T.K., supervised A.D.S. and manuscript input; T.B., supervised S.S. and D.P.-A., and wrote the manuscript.

COMPETING INTERESTS

The authors declare no conflict of interest.

ADDITIONAL INFORMATION

Supplementary figures are available as Supporting Information for this paper.

DATA AVAILABILITY

Key lab materials, protocols, data, and code used and generated in this study are listed in the Supporting Information in a Key Resource Table alongside their persistent identifiers.

REFERENCES

1. Poewe W*, et al.* Parkinson disease. *Nat Rev Dis Primers* **3**, 17013 (2017).

2. Halliday GM, Leverenz JB, Schneider JS, Adler CH. The neurobiological basis of cognitive impairment in Parkinson's disease. *Mov Disord* **29**, 634-650 (2014).

3. Aarsland D*, et al.* Parkinson disease-associated cognitive impairment. *Nat Rev Dis Primers* **7**, 47 (2021).

4. Hely MA, Reid WG, Adena MA, Halliday GM, Morris JG. The Sydney multicenter study of Parkinson's disease: the inevitability of dementia at 20 years. *Mov Disord* **23**, 837-844 (2008).

5. Buter TC, van den Hout A, Matthews FE, Larsen JP, Brayne C, Aarsland D. Dementia and survival in Parkinson disease: a 12-year population study. *Neurology* **70**, 1017-1022 (2008).

6. Li J*, et al.* Cortical and subcortical morphological alterations in motor subtypes of Parkinson's disease. *NPJ Parkinsons Dis* **8**, 167 (2022).

7. Caviness JN*, et al.* Parkinson's disease, cortical dysfunction, and alpha-synuclein. *Mov Disord* **26**, 1436-1442 (2011).

8. Bruck A, Aalto S, Nurmi E, Bergman J, Rinne JO. Cortical 6-[18F]fluoro-L-dopa uptake and frontal cognitive functions in early Parkinson's disease. *Neurobiol Aging* **26**, 891-898 (2005).

9. Schapira AHV, Chaudhuri KR, Jenner P. Non-motor features of Parkinson disease. *Nat Rev Neurosci* **18**, 435-450 (2017).

10. Ryman SG*, et al.* Cognition at Each Stage of Lewy Body Disease with Co-occurring Alzheimer's Disease Pathology. *J Alzheimers Dis* **80**, 1243-1256 (2021).

11. Irwin DJ*, et al.* Neuropathological and genetic correlates of survival and dementia onset in synucleinopathies: a retrospective analysis. *Lancet Neurol* **16**, 55-65 (2017).

12. Irwin DJ*, et al.* Neuropathologic substrates of Parkinson disease dementia. *Ann Neurol* **72**, 587-598 (2012).

13. Braak H, Rub U, Del Tredici K. Cognitive decline correlates with neuropathological stage in Parkinson's disease. *J Neurol Sci* **248**, 255-258 (2006).

14. Jellinger KA. Lewy body-related alpha-synucleinopathy in the aged human brain. *J Neural Transm (Vienna)* **111**, 1219-1235 (2004).

15. Marui W*, et al.* Progression and staging of Lewy pathology in brains from patients with dementia with Lewy bodies. *J Neurol Sci* **195**, 153-159 (2002).

16. Gomez-Tortosa E, Newell K, Irizarry MC, Albert M, Growdon JH, Hyman BT. Clinical and quantitative pathologic correlates of dementia with Lewy bodies. *Neurology* **53**, 1284-1291 (1999).

17. Benussi A, Pilotto A, Cantoni V, Ferrari E, Borroni B, Padovani A. Neurophysiological Correlates of Motor and Cognitive Dysfunction in Prodromal and Overt Dementia with Lewy Bodies. *J Alzheimers Dis* **86**, 579-588 (2022).

18. Halliday GM, McCann H. The progression of pathology in Parkinson's disease. *Ann N Y Acad Sci* **1184**, 188-195 (2010).

19. Howlett DR*, et al.* Regional Multiple Pathology Scores Are Associated with Cognitive Decline in Lewy Body Dementias. *Brain Pathol* **25**, 401-408 (2015).

20. Braak H, Del Tredici K, Rub U, de Vos RA, Jansen Steur EN, Braak E. Staging of brain pathology related to sporadic Parkinson's disease. *Neurobiol Aging* **24**, 197-211 (2003).

21. Goralski TM*, et al.* Spatial transcriptomics reveals molecular dysfunction associated with cortical Lewy pathology. *Nature Communications* **15**, 2642 (2024).

22. Henderson MX, Henrich MT, Geibl FF, Oertel WH, Brundin P, Surmeier DJ. The roles of connectivity and neuronal phenotype in determining the pattern of alpha-synuclein pathology in Parkinson's disease. *Neurobiol Dis* **168**, 105687 (2022).

23. Morris HR, Spillantini MG, Sue CM, Williams-Gray CH. The pathogenesis of Parkinson's disease. *Lancet* **403**, 293-304 (2024).

24. Stoyka LE*, et al.* Behavioral defects associated with amygdala and cortical dysfunction in mice with seeded alpha-synuclein inclusions. *Neurobiol Dis* **134**, 104708 (2020).

25. Calo L, Wegrzynowicz M, Santivanez-Perez J, Grazia Spillantini M. Synaptic failure and alpha-synuclein. *Mov Disord* **31**, 169-177 (2016).

26. Vargas KJ*, et al.* Synucleins have multiple effects on presynaptic architecture. *Cell Rep* **18**, 161-173 (2017).

27. Zhan SS, Beyreuther K, Schmitt HP. Quantitative assessment of the synaptophysin immuno-reactivity of the cortical neuropil in various neurodegenerative disorders with dementia. *Dementia* **4**, 66-74 (1993).

28. Andersen KB*, et al.* Reduced Synaptic Density in Patients with Lewy Body Dementia: An [(11) C]UCB-J PET Imaging Study. *Mov Disord* **36**, 2057-2065 (2021).

29. Holmes SE*, et al.* Synaptic loss and its association with symptom severity in Parkinson's disease. *NPJ Parkinsons Dis* **10**, 42 (2024).

30. Frigerio I*, et al.* Regional differences in synaptic degeneration are linked to alpha-synuclein burden and axonal damage in Parkinson's disease and dementia with Lewy bodies. *Acta Neuropathol Commun* **12**, 4 (2024).

31. Kramer ML, Schulz-Schaeffer WJ. Presynaptic alpha-synuclein aggregates, not Lewy bodies, cause neurodegeneration in dementia with Lewy bodies. *J Neurosci* **27**, 1405-1410 (2007).

32. Blumenstock S*, et al.* Seeding and transgenic overexpression of alpha-synuclein triggers dendritic spine pathology in the neocortex. *EMBO Mol Med* **9**, 716-731 (2017).

33. Henderson MX*, et al.* Spread of alpha-synuclein pathology through the brain connectome is modulated by selective vulnerability and predicted by network analysis. *Nat Neurosci* **22**, 1248-1257 (2019).

34. Luk KC*, et al.* Pathological alpha-synuclein transmission initiates Parkinson-like neurodegeneration in nontransgenic mice. *Science* **338**, 949-953 (2012).

35. Chen L, Chehade HD, Chu HY. Motor cortical neuronal hyperexcitability associated with alpha-synuclein aggregation. *NPJ Parkinsons Dis* **11**, 18 (2025).

36. Volpicelli-Daley LA*, et al.* Exogenous alpha-synuclein fibrils induce Lewy body pathology leading to synaptic dysfunction and neuron death. *Neuron* **72**, 57-71 (2011).

37. Chu HY*, et al.* Dysfunction of motor cortices in Parkinson's disease. *Cereb Cortex* **34**, (2024).

38. Okuzumi A*, et al.* Rapid dissemination of alpha-synuclein seeds through neural circuits in an in-vivo prion-like seeding experiment. *Acta Neuropathol Commun* **6**, 96 (2018).

39. Sauerbeck AD*, et al.* SEQUIN multiscale imaging of mammalian central synapses reveals loss of synaptic connectivity resulting from diffuse traumatic brain injury. *Neuron* **107**, 257-273 e255 (2020).

40. Gcwensa NZ*, et al.* Excitatory synaptic structural abnormalities produced by templated aggregation of alpha-syn in the basolateral amygdala. *Neurobiol Dis* **199**, 106595 (2024).

41. Koopmans F*, et al.* SynGO: an evidence-based, expert-curated knowledge base for the synapse. *Neuron* **103**, 217-234 e214 (2019).

42. Shepherd GM. Corticostriatal connectivity and its role in disease. *Nat Rev Neurosci* **14**, 278-291 (2013).

43. Pérez-Acuña D, Shin SJ, Rhee KH, Kim SJ, Lee SJ. alpha-Synuclein propagation leads to synaptic abnormalities in the cortex through microglial synapse phagocytosis. *Mol Brain* **16**, 72 (2023).

44. Chen L*, et al.* Synaptic location is a determinant of the detrimental effects of alpha-synuclein pathology to glutamatergic transmission in the basolateral amygdala. *Elife* **11**, (2022).

45. Tang S*, et al.* Large-scale network dysfunction in alpha-Synucleinopathy: A meta-analysis of resting-state functional connectivity. *EBioMedicine* **77**, 103915 (2022).

46. Gorges M*, et al.* To rise and to fall: functional connectivity in cognitively normal and cognitively impaired patients with Parkinson's disease. *Neurobiol Aging* **36**, 1727-1735 (2015).

47. Vargas KJ, Colosi PL, Girardi E, Park JM, Harmon LE, Chandra SS. alpha-Synuclein colocalizes with AP180 and affects the size of clathrin lattices. *J Biol Chem* **299**, 105091 (2023).

48. Nemani VM*, et al.* Increased expression of alpha-synuclein reduces neurotransmitter release by inhibiting synaptic vesicle reclustering after endocytosis. *Neuron* **65**, 66-79 (2010).

49. Wu Q, Takano H, Riddle DM, Trojanowski JQ, Coulter DA, Lee VM. alpha-Synuclein (alphaSyn) Preformed Fibrils Induce Endogenous alphaSyn Aggregation, Compromise Synaptic Activity and Enhance Synapse Loss in Cultured Excitatory Hippocampal Neurons. *J Neurosci* **39**, 5080-5094 (2019).

50. Wu Q*, et al.* Neuronal activity modulates alpha-synuclein aggregation and spreading in organotypic brain slice cultures and in vivo. *Acta Neuropathol* **140**, 831-849 (2020).

51. Froula JM*, et al.* alpha-Synuclein fibril-induced paradoxical structural and functional defects in hippocampal neurons. *Acta Neuropathol Commun* **6**, 35-48 (2018).

52. Blumenstock S*, et al.* Cortical circuit dysfunction in a mouse model of alpha-synucleinopathy in vivo. *Brain Commun* **3**, fcab273 (2021).

53. Schirinzi T*, et al.* Early synaptic dysfunction in Parkinson's disease: Insights from animal models. *Mov Disord* **31**, 802-813 (2016).

54. Volpicelli-Daley LA, Luk KC, Lee VM. Addition of exogenous alpha-synuclein preformed fibrils to primary neuronal cultures to seed recruitment of endogenous alpha-synuclein to Lewy body and Lewy neurite-like aggregates. *Nat Protoc* **9**, 2135-2146 (2014).

55. Bousset L*, et al.* Structural and functional characterization of two alpha-synuclein strains. *Nature Communications* **4**, 2575-2588 (2013).

56. Reitz SJ, Sauerbeck AD, Kummer TT. SEQUIN: An imaging and analysis platform for quantification and characterization of synaptic structures in mouse. *STAR Protoc* **2**, 100268 (2021).

57. Fixemer S*, et al.* Microglia phenotypes are associated with subregional patterns of concomitant tau, amyloid-beta and alpha-synuclein pathologies in the hippocampus of patients with Alzheimer's disease and dementia with Lewy bodies. *Acta Neuropathol Commun* **10**, 36 (2022).

58. Ke G*, et al.* Lightgbm: A highly efficient gradient boosting decision tree. In: *Advances in Neural Information Processing Systems*) (2017).

59. Imbrosci B, Schmitz D, Orlando M. Automated Detection and Localization of Synaptic Vesicles in Electron Microscopy Images. *eNeuro* **9**, (2022).

60. Hänzelmann S, Castelo R, Guinney J. GSVA: gene set variation analysis for microarray and RNA-seq data. *BMC Bioinformatics* **14**, 7 (2013).

61. Danaher P*, et al.* Advances in mixed cell deconvolution enable quantification of cell types in spatial transcriptomic data. *Nature Communications* **13**, 385-398 (2022).

62. Pologruto TA, Yasuda R, Svoboda K. Monitoring neural activity and [Ca2+] with genetically encoded Ca2+ indicators. *J Neurosci* **24**, 9572-9579 (2004).

905 **FIGURE LEGENDS**

906

907 **Figure 1. Progressive loss of intracortical excitatory synapses in the PFF model of α-synucleinopathy.**

908 **a** Diagram of striatal injection of α-syn pre-formed fibrils (PFFs) in mice, resulting in progressive pathology
909 in cortical neurons projecting to the striatum. Injection of α-syn monomer served as control.

910 **b** Representative 3D high-resolution immunostainings acquired by Airyscan imaging in layer V of frontal
911 cortex, secondary motor area M2. Tissue was immunostained for excitatory presynaptic VGLUT1 (green)
912 and excitatory postsynaptic Homer (red). VGLUT1 marks intracortical synapses. Staining for phospho-α-
913 syn (p-α-syn, magenta) detects α-syn aggregates. Images were acquired 1 month post-injection (MPI) of
914 monomer (left) or PFF (right) and processed for SEQUIN analysis. Scale bar, 5 µm.

915 **c** The density of synapses marked by spatially paired VGLUT1 and Homer specializations was unchanged
916 at 1 MPI of monomer vs. PFF. The frequency distribution of nearest-neighbor VGLUT1/Homer pairs was
917 calculated from images as in (**b**). (n=5 animals/group, 6-8 slices per animal)

918 **d** No reduction in the density of total excitatory pre- and post-synaptic specializations was observed 1
919 MPI. Images as in (**b**) were analyzed. Analysis included isolated and synaptically paired VGLUT1 and Homer
920 puncta.

921 **e** Airyscan imaging of VGLUT1 and Homer with staining for p-α-syn was performed in the frontal cortex
922 layer V as in (**b**) at 3 MPI of monomer or PFF.

923 **f** Excitatory synapse loss occurred at 3 MPI of PFF compared to monomer. Quantification as in (**c**). (n=5
924 animals/group, monomer 6-10 and PFF 6-8 slices per animal)

925 **g** The total number of individual excitatory pre- and post-synaptic specializations, including isolated and
926 synaptically paired VGLUT1 and Homer puncta, was reduced at 3 MPI.

927 **h** Airyscan imaging of VGLUT1 and Homer with staining for p-α-syn was performed in the frontal cortex
928 layer V as in (**b**) at 6 MPI of monomer or PFF.

929 **i** Excitatory synapse loss persisted at 6 MPI of PFF compared to monomer. Image quantification as in (**c**).
930 (n=6 animals/group, 6-8 slices per animal).

931 **j** The number of total excitatory pre- and post-synaptic specializations, including isolated and synaptically
932 paired VGLUT1 and Homer puncta, was increased at 6 MPI.

933 Results are presented as mean ± SEM and considered statistically significant with $p<0.05$ after unpaired
934 parametric t-test. Tissue slices for each time point were processed in parallel.

935

936 **Figure 2. Synuclein pathology impacts the structural properties of excitatory synapses.**

937 **a** Representative high-resolution Airyscan images from the frontal cortex M2 layer V. Images were
938 acquired 3 MPI of monomer control (left) or PFF (right) and show paired pre- and post-synaptic
939 excitatory VGLUT1 (green) and Homer (red) specializations, with p-α-syn in magenta. Scale bar, 1 µm.

940 **b** VGLUT1/Homer specializations become spatially separated in PFF- compared to monomer control-
941 injected mice. Nearest-neighbor separation distances were determined from images as (**a**) by analyzing
942 the Gaussian distribution of synaptically paired puncta and their mean distance.

943 **c** The separation of spatially paired VGLUT1/Homer specializations measured from images as in (**a**) was
944 increased in PFF- compared to monomer control-injected mice. The graph shows separation distances
945 for individual synaptic pairs after nearest-neighbor analysis. Results are presented as mean ± SEM with
946 unpaired parametric t-test. (**b,c,** n=5 animals/group, 6-10 slices per animal)

947 **d** Ultrastructural analysis of synaptic morphology in mice injected with PBS control vs. PFF at 3 MPI in
948 M2. Representative transmission electron microscopy (EM) images of synapses in the frontal cortex are
949 shown. Scale bar, 600 nm.

e,f Excitatory synapses undergo ultrastructural changes. Analysis of EM images as in (**d**) determined that synaptic cleft width (**e**) and synaptic vesicle area (**f**) were reduced. Data were analyzed after Box-Cox transformation using linear mixed models with synapses nested within each mouse. (**e**, n=8810 synaptic vesicles for the PBS group and 7576 for the PFF group from 4 mice per group; **f**, n=283 synapses for the PFF group and n=345 for the PBS group from 4 mice per group)

Figure 3. Dysregulation of synaptic pathways in α-synuclein pathology-bearing neurons.

a Volcano plot of SynGO annotated genes differentially expressed in p-α-syn pathology-bearing cortical neurons. Proteins for image quantification are noted. *Slc17a17*, VGLUT1; *Gphn*, Gephyrin; *Slc32a1*, VGAT.

b Sunburst plots of genes downregulated in pathology-bearing neurons illustrate changes in genes encoding synaptic vesicle and post-synaptic density components (left) and involved in processes relevant for synapse organization (right). DEG, differentially expressed gene.

c Bar plots show the top enriched gene ontology terms in the synaptic categories presented in (**b**).

d A smaller set of genes was upregulated in pathology-bearing neurons. They encode postsynaptic components (left) and contribute to synapse-organizing and signaling pathways (right).

Figure 4. Aggregation of α-synuclein occurs in synapses and is positively correlated with synapse loss.

a Representative 3D imaging fields for excitatory postsynaptic PSD-95 (magenta), the synaptic vesicle protein synapsin (green), and p-α-syn (cyan) in frontal cortex M2 at 1 MPI of PFFs. Scale bar, 5 µm.

b High magnification 2D projection at 600 nm thickness showing the synaptic overlap of p-α-syn with spatially paired synapsin and PSD-95. Scale bar, 1 µm.

c Schematic of measuring p-α-syn immunostaining in 200 nm fields centered on synaptic loci.

d Quantification of cortical p-α-syn in monomer-injected control mice and of synaptic and parenchymal p-α-syn in PFF-injected animals. Grey dots are data from individual image tiles, and circles show the median for each animal. Red lines mark the group-wise median values of synaptic and parenchymal p-α-syn in PFF mice, and arrowheads depict the amount of p-α-syn that is synapse-associated above parenchymal levels. (monomer, n=1019 tiles; PFF, n=196 high path area tiles from 3 mice per group)

e Representative mesoscale tilescan of excitatory postsynaptic PSD-95 (magenta) and p-α-syn (cyan) in frontal cortex at 1 MPI of monomer. A maximum intensity projection is shown. Scale bar, 1000 µm.

f,g Groupwise average heatmaps of synaptic p-α-syn abundance (**f**) and synapse density (**g**) from monomer-injected control animals in the area shown in (**e**).

h Maximum intensity projection tilescan of PSD-95 and p-α-syn at 1 MPI in a PFF-injected animal, acquired as in (**e**).

i,j Groupwise average heatmaps of synaptic p-α-syn (**i**) and synapse density (**j**) from PFF-injected animals in the area shown in (**h**).

k Synaptically localized p-α-syn from areas as in (**f,i**) was detected 1 MPI of PFF compared to monomer.

l Synapse loss is already detectable 1 MPI of PFF compared to monomer upon mesoscale analysis. Analysis was performed of areas as shown in (**g,j**).

Statistical analyses in (**k,l**) were performed on individual image tiles using a linear mixed-effects model to account for non-independent data. Box and whisker plots represent the 25-75% interquartile range, and the median is marked in the box, with whiskers showing 10th and 90th percentiles.

Figure 5. Increased phospho-α-synuclein in synapses and low synapse density proximal to α-synuclein aggregates.

a Representative image of presynaptic synapsin (green), postsynaptic PSD-95 (magenta), and p-α-syn aggregates (cyan) in the cortex 1 MPI of PFF. Scale bar, 10 µm.

b Example for processing images as in (**a**) to obtain p-α-syn aggregate masks.

c Schematic of the boxed region in (**a,b**) depicting the approach to measure distances between synaptic centroids and borders of p-α-syn aggregates.

d Quantification of images as in (**a**) shows that synaptic p-α-syn enrichment is correlated with the distance to the nearest Lewy-neurite like p-α-syn aggregate.

e Synapses were localized as visualized in (**c**) within 800 nm of p-α-syn aggregates. Aggregates were binned by the extent of their p-α-syn signal. Quantification shows that the lowest synapse density was observed proximal to the aggregates with the highest p-α-syn intensity. A within-intensity bin median calculation was used for the density measurement. (**d,e,** n=598 image tiles for monomer, n=565 PFF from 3 mice per group; Spearman's rank correlation coefficients provided in the panels)

Figure 6. α-Synuclein pathology does not impact VGLUT2-positive long-range inputs.

a Representative 3D high-resolution images obtained by Airyscan microscopy after immunostaining for excitatory presynaptic VGLUT2 (red) and postsynaptic Homer (green) in frontal cortex M2. VGLUT2 marks long-range synaptic inputs. Staining for p-α-syn detected α-syn aggregates (magenta). Images were obtained 3 MPI of monomer control (left) or PFF injection (right). Scale bar, 5 µm.

b Cortical α-syn aggregates do not impact the density of VGLUT2/Homer synapses. Synapse density was calculated after SEQUIN analysis of images as in (**a**) from the frequency distribution of nearest-neighbor VGLUT2 and Homer pairs. (n=5 animals/group, 6-8 slices per animal)

c No difference was measured in the density of total excitatory pre- and post-synaptic VGLUT2 and Homer specializations in monomer vs. PFF-injected mice. This analysis included isolated and synaptically paired puncta. Images as in (**a**) were analyzed.

d Representative high-resolution images from the cortex at 3 MPI showing paired pre- and post-synaptic VGLUT2 (green) and Homer (red). p-α-syn is shown in magenta. Tissues were obtained after injection of monomer as control (left) and PFF (right). Scale bar, 1 µm.

e Separation distances of paired VGLUT2/Homer specializations were unchanged 3 MPI of PFF compared to monomer control. Nearest-neighbor separation distances were determined from images as in (**d**) by analyzing the Gaussian distribution of VGLUT2 and Homer signals.

f Separation distances for individual synaptic VGLUT2/Homer pairs are not distinguishable after nearest-neighbor analysis for monomer control vs. PFF injection. (**e,f,** n=5 animals/group, 6-8 slices per animal)

Results are presented as mean ± SEM and considered statistically significant with $p<0.05$ after an unpaired parametric t-test.

Figure 7. Inhibitory postsynaptic Gephyrin puncta density is initially unaffected in the cortex but reduced 6 months after PFF injection.

a Representative 3D high-resolution immunostainings of inhibitory presynaptic vGAT (red) and postsynaptic Gephyrin (green) in frontal cortex M2, with p-α-syn shown in magenta. Immunostainings were obtained by Airyscan microscopy 3 MPI after monomer (left) or PFF injection (right). Scale bar, 5 µm.

b Inhibitory synapse density determined by measuring VGAT and Gephyrin puncta paired into synapses was unchanged 3 MPI PFF compared to monomer. Synaptic density was calculated from images as in (**a**) using SEQUIN by nearest-neighbor analyses of puncta. (n=3 animals/group, 6-7 slices per animal)

c Analysis of images as in (**a**) did not show a difference in total VGAT (left) or Gephyrin puncta density (right) at 3 MPI PFF compared to monomer. This analysis included isolated and synaptically paired puncta.

d Images of VGAT and Gephyrin specializations were obtained at 6 MPI of monomer or PFF as in (**a**).

e No change in inhibitory synapse density was observed 6 MPI monomer compared to PFF after analysis of images as in (**d**).

f VGAT puncta were unchanged 6 MPI of monomer vs. PFF (left), but the number of Gephyrin puncta was reduced after PFF injection (right). Images as in (**d**) were analyzed. (5 monomer and 4 PFF-injected animals with n=6-8 slices per animal)

Results are presented as mean ± SEM and considered statistically significant with $p<0.05$ after an unpaired parametric t-test.

Figure 8. Intracortical pathology across layers and correlated synapse loss within columns.

a Simplified schematic of intracortical connectivity between layers II/III and V in the mouse cortex. Red arrows indicate direction of pathology spread. Adapted from Shepherd (2013) [42].

b Representative mesoscan from a PFF-injected animal 1 MPI showing PSD-95 (magenta) and p-α-syn (cyan). Section-specific registration to the Allen Brain Atlas is shown in solid lines. Images were acquired in secondary motor cortex M2 and anterior cingulate.

c Mixed effects model analysis of synapse density data of combined layers V and II/III from images as in (**b**). (layer V: monomer, n=304 tiles, PFF, n=285 tiles; layer II/III: monomer, n=191 tiles, PFF, n=185 tiles; from 3 animals per group)

d Quantification of individual synaptic densities in layer V and layer II/III of monomer- and PFF-injected animals from images as in (**b**). (layer V: monomer, n=112 tiles, PFF, n=110 tiles; layer II/III: monomer, n=100 tiles, PFF, n=93 tiles from 3 animals per group; Mann-Whitney test on individual layers) Box and whisker plots in (**c,d**) represent the 25-75% interquartile range, and the median is marked in the box, with whiskers showing 10th and 90th percentiles.

e Representative image from a PFF-treated animal at 1 MPI showing presynaptic synapsin (green), PSD-95 (magenta) and p-α-syn (cyan). Section-specific registration to the Allen Brain Atlas is shown in solid lines. The region shown corresponds to the boxed region in (**b**).

f Quantification of synaptic p-α-syn immunoreactivity in layer II/III and layer V of PFF-injected animals shows that it is correlated within individual cortical columns. Images as in (**e**) were analyzed.

g Strong correlation of synaptic density in layers II/III and V within cortical columns after PFF injection. Images as in (**e**) were analyzed. (**f,g;** n=3-4 cortical columns per animal from 3 animals; Pearson correlation coefficients provided in the panels)

Figure 9. α-Synuclein pathology and loss of excitatory VGLUT1-positive synapses in the cortical hemisphere contralateral to PFF injection.

a Schematic of IT and PT neuron connectivity. IT neurons (grey) project ipsilaterally to the striatum and to the contralateral striatum and cortex. PT neurons (green) project only ipsilaterally to the striatum. Red arrows indicate the direction of α-syn pathology spread. Adapted from Shepherd (2013) [42].

b Representative tiled confocal images showing p-α-syn immunostaining (white) in cortical hemispheres ipsilateral and contralateral to the striatal PFF injection site, co-stained with DAPI (blue). p-α-syn-positive aggregates are observed in layer V of the contralateral side at 6 MPI. Scale bar: 5 mm.

c Representative 3D high-resolution images from layer V of the frontal cortex M2 contralateral to the striatum unilaterally injected with PFFs. Images were acquired using Airyscan. Tissue was immunostained for excitatory presynaptic VGLUT1 (green), postsynaptic Homer (red), and p-α-syn (magenta). Images were acquired at 6 MPI following injection of monomer (left) or PFF (right) and processed for SEQUIN analysis. Scale bar: 5 µm.

d Excitatory synaptic density, defined by spatially paired VGLUT1 and Homer specializations, was reduced in the contralateral frontal cortex after ipsilateral PFF injection compared to monomer. Quantification was performed from images as in (**c**) by analyzing the frequency distribution of nearest-neighbor VGLUT1/Homer pairs. (n=6 animals/group, 6–8 slices per animal)

1088 **e** No reduction was observed in the density of total excitatory pre- and post-synaptic specializations in
1089 the contralateral cortex. Images as in (**c**) were analyzed. (n=6 animals/group, 6–8 slices per animal)

1090

1091 **Figure 10. Reduction in frequency of miniature excitatory synaptic currents in mice with PFF injection.**

1092 **a** Traces showing miniature excitatory synaptic currents (mEPSCs, top) and miniature inhibitory currents
1093 (mIPSCs, bottom) recorded from pyramidal cells in monomer (left) or PFF (right) injected mice.

1094 **b** Scatter plots of current amplitudes for mEPSCs and mIPSCs. No difference was observed in the event
1095 amplitude of mEPSCs or mIPSC between monomer- and PFF-injected mice.

1096 **c** Scatter plots of inter-event interval for mEPSCs and mIPSCs from monomer and PFF-injected mice.
1097 Inter-event interval was significantly higher for mEPSCs from PFF-injected mice (n=12 cells from 6 mice)
1098 than after monomer injection (n=8 cells from 3 mice). No difference was seen in the inter-event interval
1099 for mIPSCs. (9=cells from 6 PFF injected mice; n=8 cells from 3 monomer injected mice)

1100 Results are presented as mean ± SEM and considered statistically significant with $p<0.05$, after an
1101 unpaired t-test.

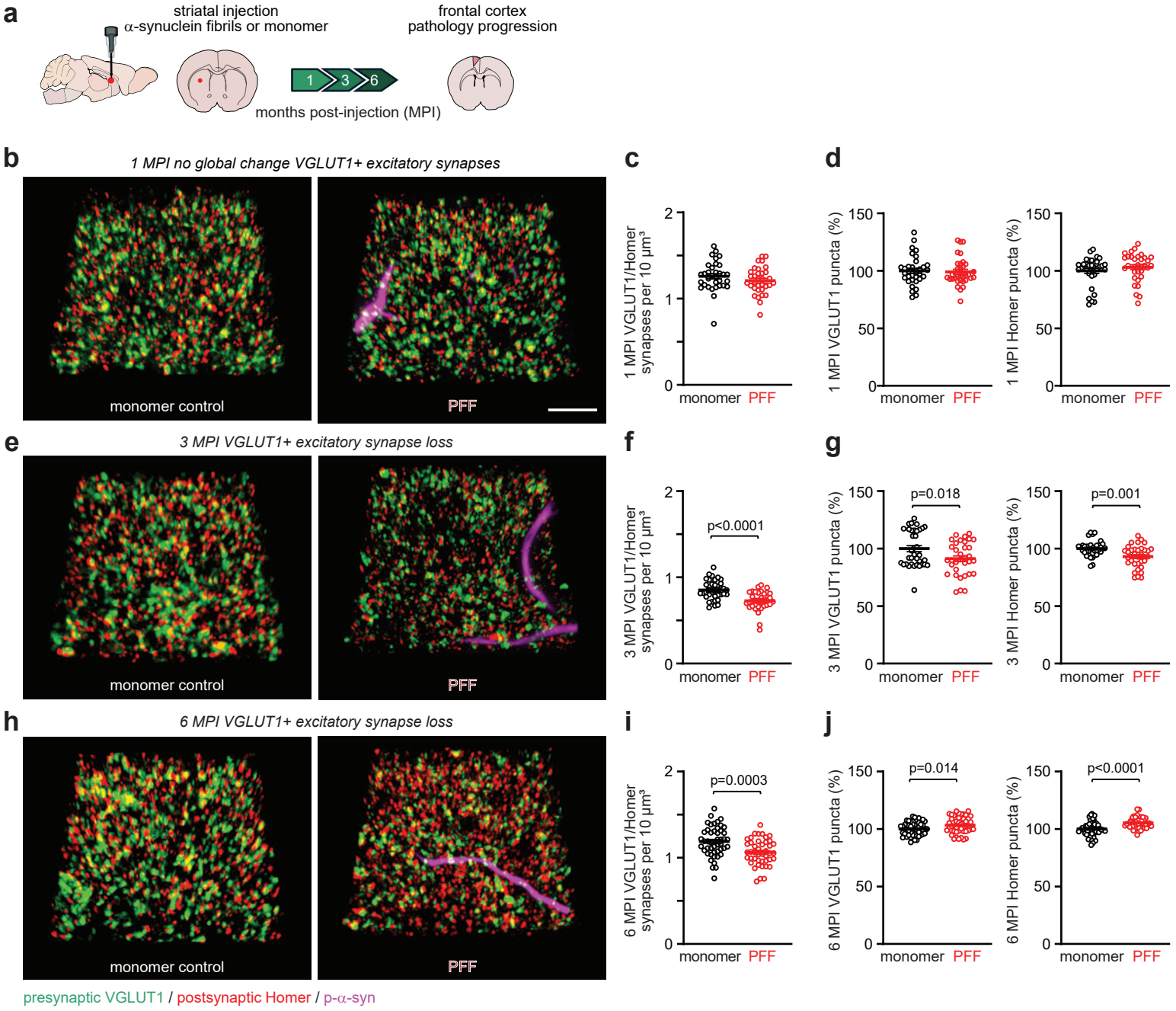

Figure 1. Progressive loss of intracortical excitatory synapses in the PFF model of α-synucleinopathy.

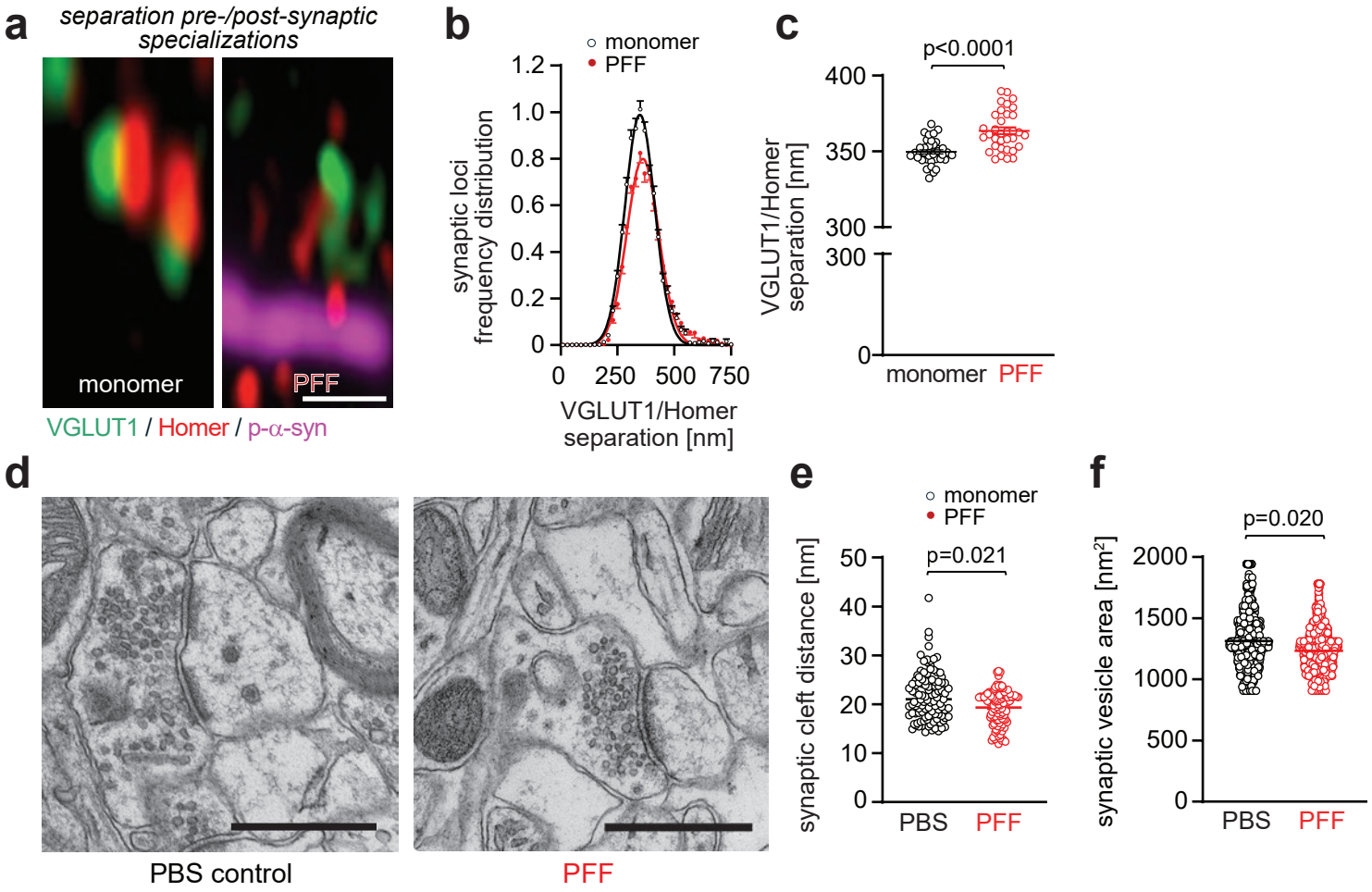

Figure 2. Synuclein pathology impacts the structural properties of excitatory synapses.

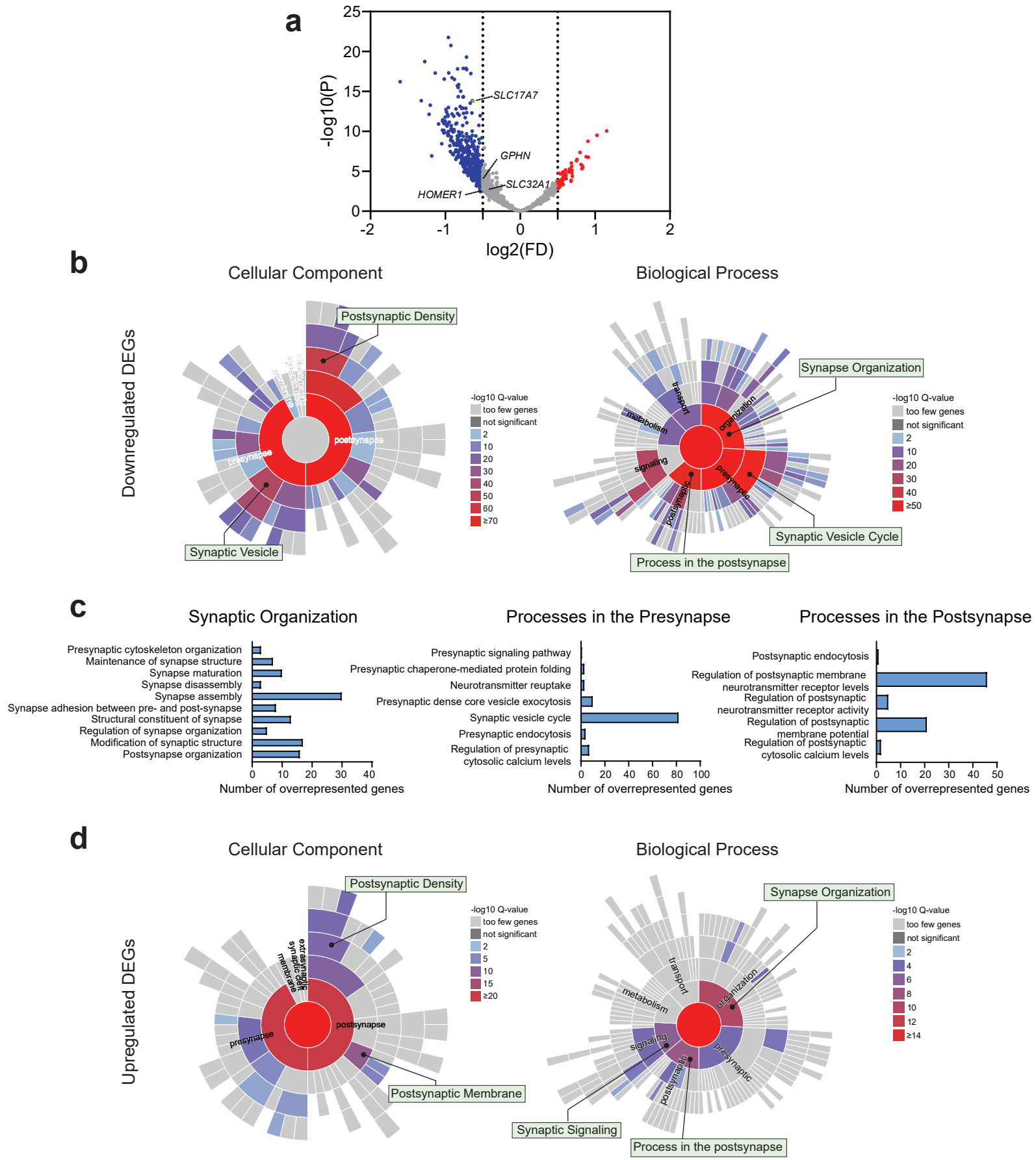

Figure 3. Dysregulation of synaptic pathways in α-synuclein pathology-bearing neurons.

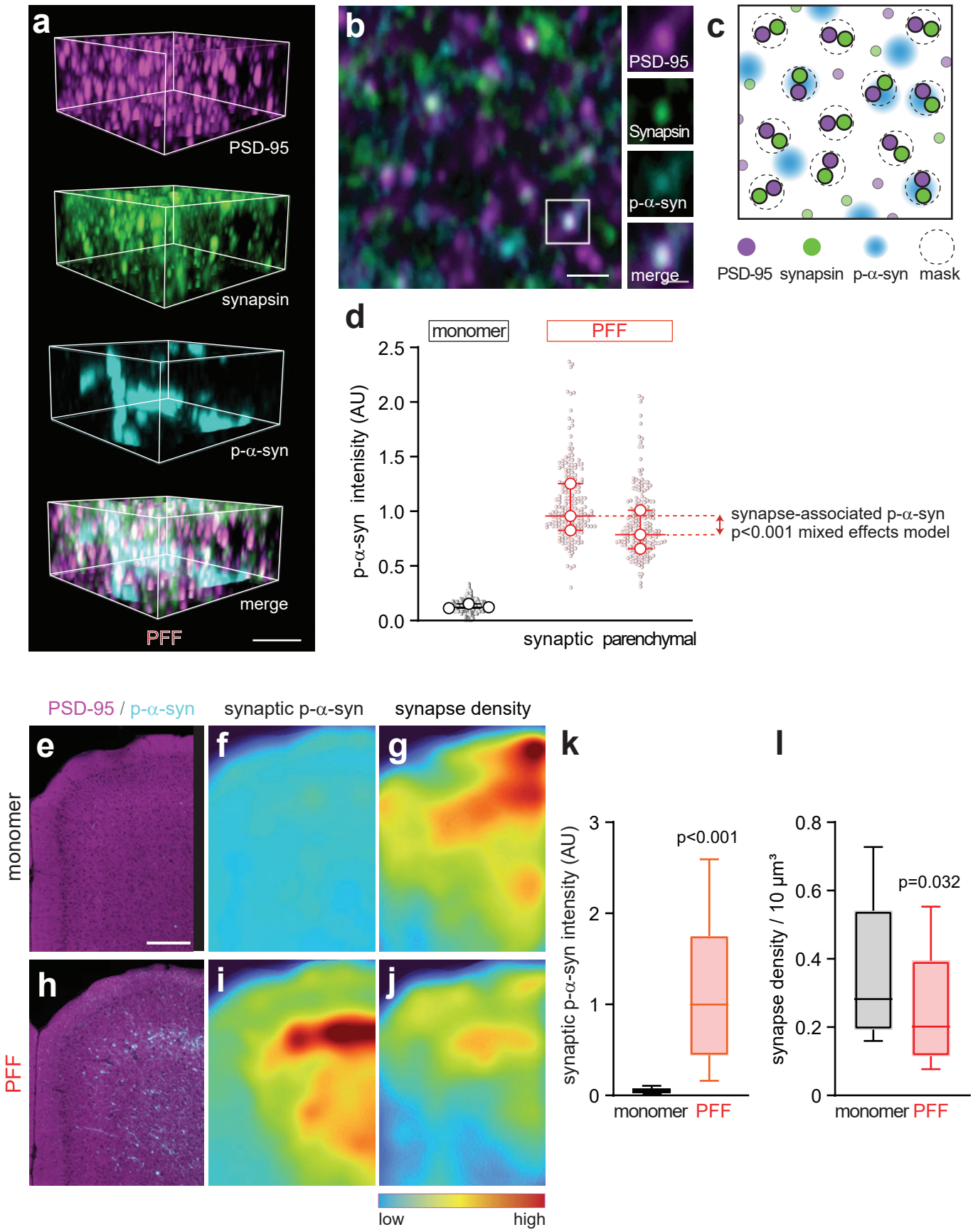

Figure 4. Aggregation of α-synuclein occurs in synapses and is positively correlated with synapse loss.

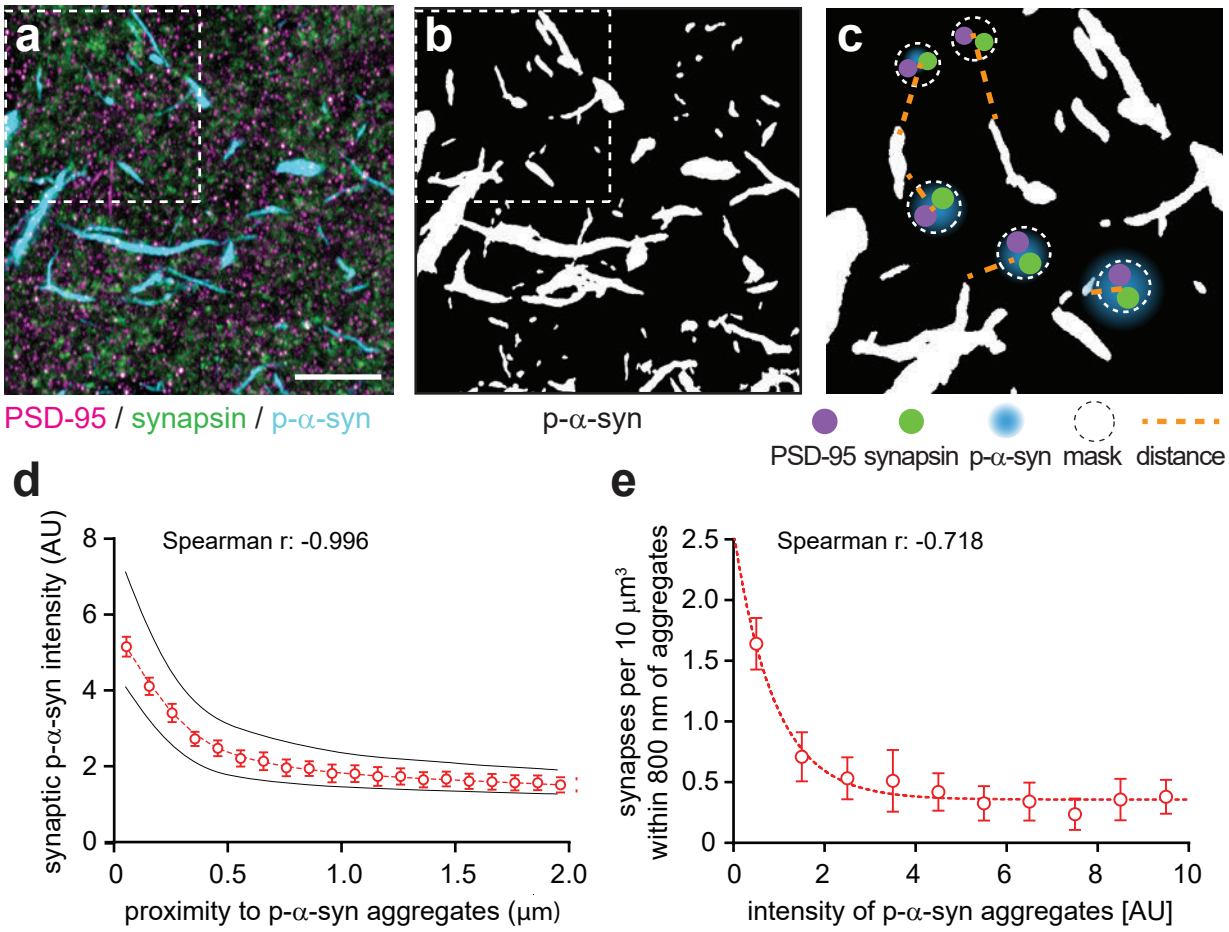

Figure 5. Increased phospho-α-synuclein in synapses and low synapse density proximal to α-synuclein aggregates.

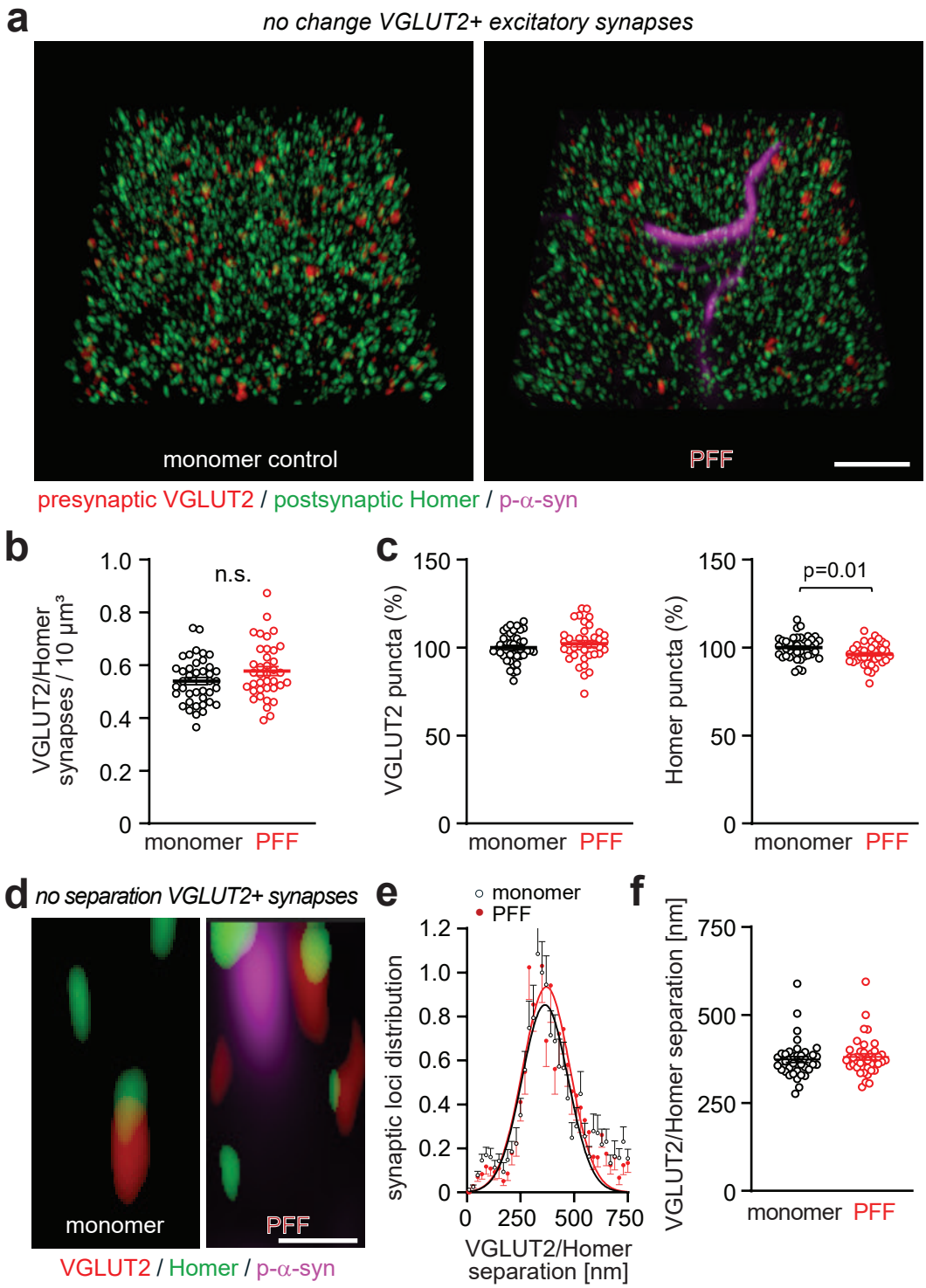

Figure 6. α-Synuclein pathology does not impact VGLUT2-positive long-range inputs.

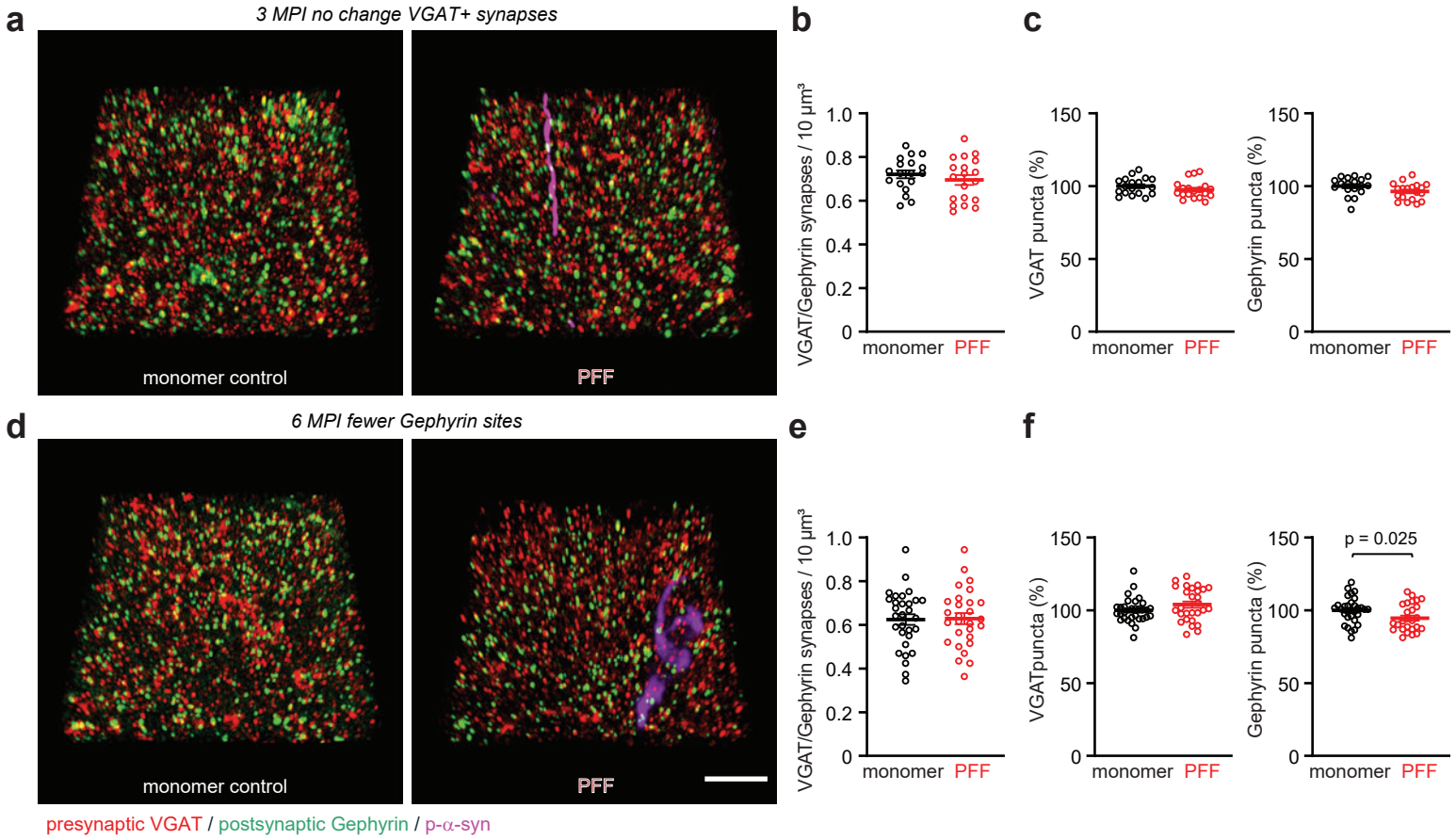

Figure 7. Inhibitory postsynaptic Gephyrin puncta density is initially unaffected in the cortex but reduced 6 months after PFF injection.

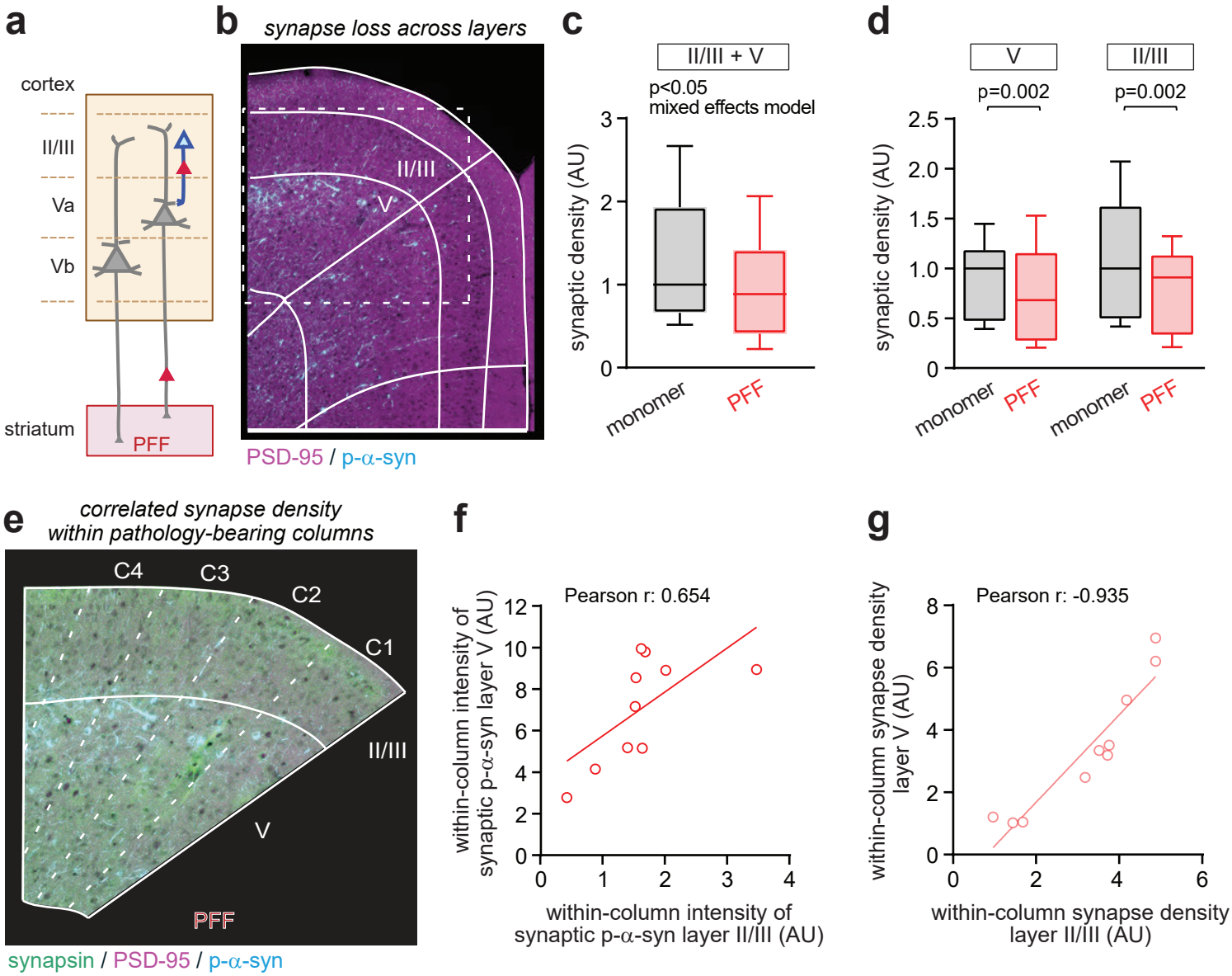

Figure 8. Intracortical synapse loss occurs in layers II/III and V and is correlated within columns.

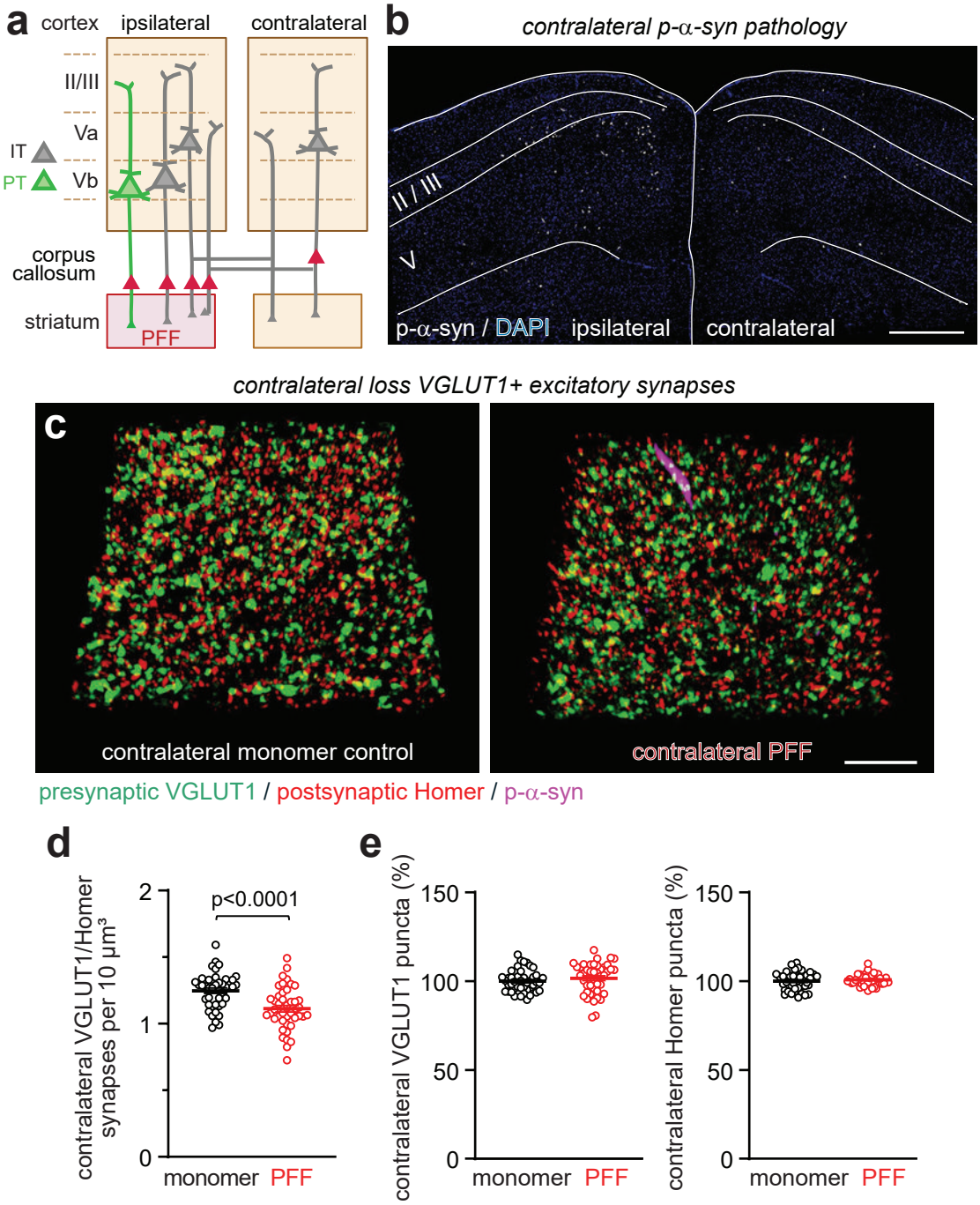

Figure 9. α-Synuclein pathology and loss of excitatory VGLUT1-positive synapses in the cortical hemisphere contralateral to PFF injection.

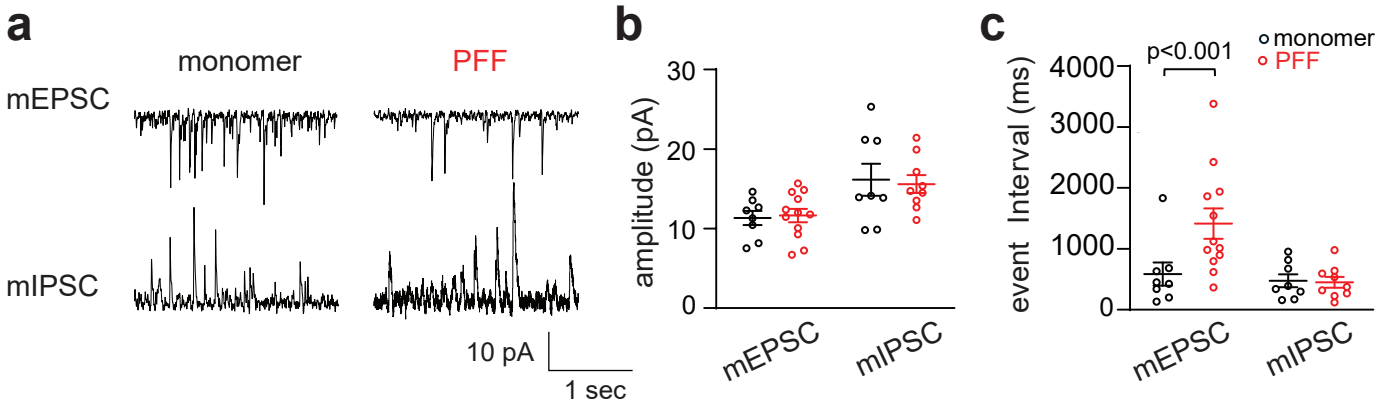

Figure 10. Reduction in frequency of miniature excitatory synaptic currents in mice with PFF injection.